Non-linear dynamics of a mechanical system with a frictional unilateral constraint

Giovanni Lancioni, Stefano Lenci, Ugo Galvanetto

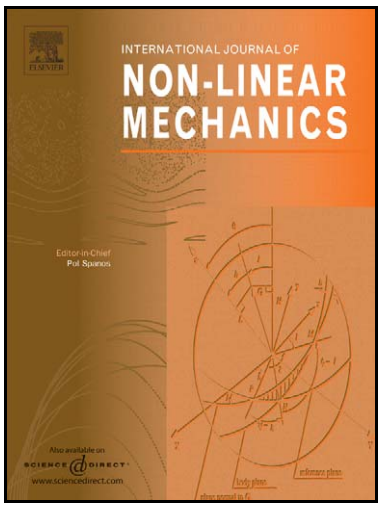

www.elsevier.com/locate/nlm

Non-linear dynamics of a mechanical system with a frictional unilateral constraint

Giovanni Lancioni, Stefano Lenci, Ugo Galvanetto

PII: S0020-7462(09)00039-0
DOI: doi:10.1016/j.ijnonlinmec.2009.02.012
Reference: NLM 1591

To appear in: *International Journal of Non-Linear Mechanics*

Received date: 19 October 2007
Revised date: 21 January 2009
Accepted date: 13 February 2009

Cite this article as: Giovanni Lancioni, Stefano Lenci and Ugo Galvanetto, Non-linear dynamics of a mechanical system with a frictional unilateral constraint, *International Journal of Non-Linear Mechanics* (2009), doi:10.1016/j.ijnonlinmec.2009.02.012

Non-linear dynamics of a mechanical system with a frictional unilateral constraint

Giovanni Lancioni
Stefano Lenci
Dipartimento di Architettura, Costruzioni e Strutture,
Universitá Politecnica delle Marche,
Via Brecce Bianche 1, 60131 Ancona, Italy
e-mail: g.lancioni@univpm.it, lenci@univpm.it

Ugo Galvanetto
Dipartimento di Costruzioni e Trasporti, Universitá di Padova,
Via Marzolo 9, 35131 Padova, Italy
e-mail: u.galvanetto@unipd.it

February 19, 2009

Abstract

We analyze the dynamics of a two-dimensional system constituted by two masses subjected to elastic, gravitational and viscous forces and constrained by a moving frictional mono-lateral surface. The model exhibits a time-varying dynamics capable of reproducing the hopping phenomenon, an unwanted phenomenon observed in many applications such as the motion of a robotic arm on a surface or that of a wiper on a windscreen. The system dynamics, besides being affected by geometrical non-linearities, has a non-smooth nature due to the impact and friction laws involved in the model. The complexity of the resulting equations and of the transition conditions require the problem to be solved numerically. Various periodic motions are found and

the effect of varying the system parameters, in particular the friction coefficient, is investigated. Finally simulations are used to gain some insight the behaviour of the windscreen wiper.

1 Introduction

The motion of the planar mass-spring-damper system depicted in the Fig. 1 is investigated. It consists of two masses m_1 and m_2 which are immersed in a vertical downward gravitational field and are constrained by elastic springs, viscous dashpots and a moving mono-lateral frictional surface. This model, due to [12] where it has been proposed, studied in detail and called Frictional Impact Oscillator, reproduces the hopping phenomenon observed in many applications, such as the motion of a piece of chalk pushed over a blackboard or that of a robotic arm on a plane. The system can also be seen as a simplified model of the transverse section of a wiper blade moving on the windscreen of a car, a problem which originally motivates this work [3, 8, 23]. The investigation of the dynamics is useful to understand the causes of the hopping and, as a result, to suggest the appropriate remedies to avoid this unwanted motion.

Despite its apparent simplicity, the model is very intricate due to various non-linearities involved in its dynamics. Large amplitude oscillations of mass m_1, its impacts with the moving surface and friction, acting between m_1 and the moving surface when they are in contact, are all sources of non-linear behaviour. Systems with impact and/or friction, as well as stick-slip systems have been the subject of extensive investigations due to the variety of non-linear dynamics phenomena they experience [1, 4, 6, 7, 9, 13, 14, 17, 20].

The model can be classified as a time-varying system, because its dynamics is divided in three different regimes, each characterized by a different number of degrees of freedom (dof). The free-flight motion occurs when the mass m_1 is detached from the constraining surface, and it is governed by two kinematic parameters (y and φ in Fig. 1). When m_1 is in contact we can have slipping or sticking, depending on the value of the friction force. The slip motion is governed by one dof, while in the stick motion there are no dof, and the dynamics is determined by the velocity of the moving surface.

The equations of motion are equipped with appropriate laws of transitions from one regime to the others, which are the key-points of the model, and which require an accurate modeling. In particular, for the impact of m_1 on

the surface, we adopt Poisson's law proposed in [21] and analyzed in [22], where the introduction of restitution impulses allows for the bouncing of mass m_1. The perfectly plastic impact law considered in [12] is obtained as a particular case when the normal restitution coefficient is set equal to zero. Also an infinite sequence of impacts of decreasing amplitude in finite time are possible in the model. They represent the normal transition from free-flight to contact motions.

Depending on the values of the parameters and on the state of the system, the problem can admit no solution or multiple solutions in transitions from one regime to another. This may occur in various circumstances, some of which correspond to the classical Painlevé paradox [12]. The detailed study of these situations, which entails (*i*) performing further investigations to check whether the multiplicity of the solution is only apparent and can be ruled out by theoretical proofs, or (*ii*) improving the model to eliminate its inconsistencies (by considering, for example, tangential impacts as done in [15] and experimentally verified in [24]) is out of the scopes of the present paper and is left for future works. In all examples shown in Sect. 6 we simply check in every transition that the obtained solution is unique and end the simulations if it is not.

Due to the complexity of the model, the dynamical response of the system is mainly investigated numerically with the combined use of time-histories, phase portraits, bifurcation diagrams. The goal of these simulations is that of determining, although in a preliminary way, the main aspects of the system non-linear dynamics, including various phenomena such as multistability, and smooth and non-smooth bifurcations.

Contrarily to what has been often done in the literature [12, 21, 22], we allow the moving surface to have an arbitrary - and not only constant - velocity. In particular, harmonic surface motion is considered because it simulates more realistically the motion of a windscreen wiper. In this case, the most interesting part of the dynamics occurs when the velocity changes sign. This is very important also from a practical point of view, because it is just in this situation that most unwanted phenomena are observed [19].

The paper is organized as follows. We provide in Sect. 2 the general framework for the equations of motion of the mechanical system of Fig. 1. The three different regimes of motion and the relevant transition conditions are described in Sects. 3-5. Then, we present in Sect. 6 a series of numerical simulations aimed at highlighting the main dynamical phenomena. The paper ends with the conclusions and hints for further developments (Sect.

7).

2 Equations of motion

For the plane two-mass system represented in Fig. 1, the states chosen to describe the motion are the rotation φ of the rigid bar which connects the masses m_1 and m_2, and the distance y of m_2 from the surface. They are collected in the vector $\mathbf{u} = [\varphi, y]^T$. The position, velocity and acceleration vectors of the masses m_1 and m_2 are

$$\mathbf{x}_{m_1} = \begin{bmatrix} l\sin\varphi \\ y - l\cos\varphi \end{bmatrix}; \dot{\mathbf{x}}_{m_1} = \begin{bmatrix} l\dot{\varphi}\cos\varphi \\ \dot{y} + l\dot{\varphi}\sin\varphi \end{bmatrix}; \ddot{\mathbf{x}}_{m_1} = \begin{bmatrix} -l\dot{\varphi}^2\sin\varphi + l\ddot{\varphi}\cos\varphi \\ \ddot{y} + l\dot{\varphi}^2\cos\varphi + l\ddot{\varphi}\sin\varphi \end{bmatrix}, \tag{1}$$

and

$$\mathbf{x}_{m_2} = \begin{bmatrix} 0 \\ y \end{bmatrix}; \dot{\mathbf{x}}_{m_2} = \begin{bmatrix} 0 \\ \dot{y} \end{bmatrix}; \ddot{\mathbf{x}}_{m_2} = \begin{bmatrix} 0 \\ \ddot{y} \end{bmatrix}. \tag{2}$$

Let $\dot{s}$ and $\ddot{s}$ denote the velocity and acceleration of the moving surface, respectively. We define displacement, velocity and acceleration of m_1 relative to the moving surface in the normal (N) and tangential (T) directions

$$\begin{array}{rcl} g_N &=& y - l\cos\varphi, \\ \dot{g}_N &=& \dot{y} + l\dot{\varphi}\sin\varphi, \\ \dot{g}_T &=& l\dot{\varphi}\cos\varphi - \dot{s}, \\ \ddot{g}_N &=& \ddot{y} + l\ddot{\varphi}\sin\varphi + l\dot{\varphi}^2\cos\varphi, \\ \ddot{g}_T &=& l\ddot{\varphi}\cos\varphi - l\dot{\varphi}^2\sin\varphi - \ddot{s}. \end{array} \tag{3}$$

For later use, we also define $\dot{\mathbf{g}} = [\dot{g}_N, \dot{g}_T]^T$. The kinetic energy of the system is

$$\begin{array}{rl} T &= \frac{1}{2}(m_1\dot{\mathbf{x}}_{m_1}^2 + m_2\dot{\mathbf{x}}_{m_2}^2) = \\ &= \frac{1}{2}(m_1 + m_2)\dot{y}^2 + \frac{1}{2}m_1 l^2\dot{\varphi}^2 + m_1 l\dot{\varphi}\dot{y}\sin\varphi, \end{array} \tag{4}$$

and the potential energy is

$$V = \frac{1}{2}k_y(y - y_0)^2 + \frac{1}{2}k_\varphi(\varphi - \varphi_0)^2 + m_1 g(y - l\cos\varphi) + m_2 g y, \tag{5}$$

where g is the acceleration due to gravity, k_φ and k_y are the elastic coefficients of the rotational and linear springs, and φ_0 and y_0 define the configuration of the unstressed springs. The normal and tangential contact forces between

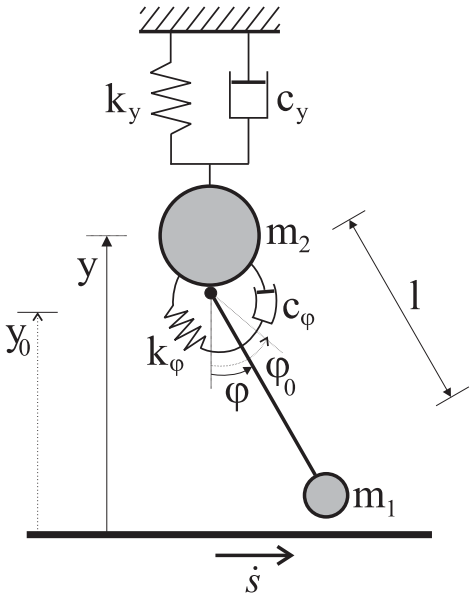

Figure 1: Frictional Impact Oscillator, see [12].

the mass m_1 and the moving surface are λ_N and λ_T, and the corresponding external work is

$$P = \lambda_N(\mathbf{x}_{m_1})_2 + \lambda_T(\mathbf{x}_{m_1})_1 = \lambda_N(y - l\cos\varphi) + \lambda_T l \sin\varphi. \tag{6}$$

The Lagrange's function is given by $\mathcal{L} = T - V + P$, and the equations of motion in the general case are

$$\frac{d}{dt}\frac{\partial \mathcal{L}}{\partial \dot{\mathbf{u}}} - \frac{\partial \mathcal{L}}{\partial \mathbf{u}} = \mathbf{f}_{nc}, \tag{7}$$

where $\mathbf{f}_{nc} = [-c_\varphi\dot{\varphi}, -c_y\dot{y}]^T$ are the non-conservative viscous forces of the rotational and linear dashpots represented in Fig. 1. The resulting two scalar equations, originally obtained also in [12], are

$$\mathbf{M}(\mathbf{u})\ddot{\mathbf{u}} = \mathbf{h}(\mathbf{u}, \dot{\mathbf{u}}) + \mathbf{F}(\mathbf{u})\mathbf{f}, \tag{8}$$

where

$$\mathbf{M} = \begin{bmatrix} m_1 l^2 & m_1 l \sin\varphi \\ m_1 l \sin\varphi & (m_1+m_2) \end{bmatrix}, \ \mathbf{F} = \begin{bmatrix} l\sin\varphi & l\cos\varphi \\ 1 & 0 \end{bmatrix},$$
$$\mathbf{h} = \begin{bmatrix} -c_\varphi\dot\varphi - k_\varphi(\varphi-\varphi_0) - m_1 g l \sin\varphi \\ -c_y\dot y - k_y(y-y_0) - m_1 l\dot\varphi^2\cos\varphi - (m_1+m_2)g \end{bmatrix}, \ \mathbf{f} = \begin{bmatrix} \lambda_N \\ \lambda_T \end{bmatrix}. \tag{9}$$

It is useful to determine explicitly the normal and tangential contact forces from (8) (note that $\mathbf{F}$ is always invertible apart from the uninteresting case $\varphi = \pm\pi/2$): $\mathbf{f} = \mathbf{F}^{-1}\mathbf{M}\ddot{\mathbf{u}} - \mathbf{F}^{-1}\mathbf{h}$. Their explicit expressions are:

$$\begin{aligned} \lambda_N &= (m_1+m_2)(\ddot y + g) + m_1 l(\ddot\varphi\sin\varphi + \dot\varphi^2\cos\varphi) + c_v\dot y + k_v(y-y_0), \\ \lambda_T &= -m_1 l\dot\varphi^2\sin\varphi + m_1 l\ddot\varphi\cos\varphi + [c_\varphi\dot\varphi + k_\varphi(\varphi-\varphi_0)]/(l\cos\varphi) + \\ &\quad + \tan\varphi[-m_2(\ddot y + g) - c_v\dot y - k_v(y-y_0)]. \end{aligned} \tag{10}$$

The problem is not yet well-defined: we have the four unknowns φ, y, λ_N and λ_T but only the two scalar equations (8). To make the problem well-posed, at least in principle, it is necessary to distinguish between different regimes of motion, and to specify contact force laws and impact laws.

The first distinction is between *free-flight*, when mass m_1 is detached from the moving surface ($g_N > 0$), and contact motions, when mass m_1 is supported by the moving surface ($g_N = 0$).

In the latter case, a further distinction is required because of the friction between the moving surface and the mass m_1. *Slip* occurs when m_1 slides on the surface ($\dot g_T \neq 0$), and *stick* when m_1 has the same velocity of the moving surface ($\dot g_T = 0$). Friction is modelled according to the classical Coulomb's law, so that when $g_N = 0$ three generic cases are possible:

$$\begin{aligned} \dot g_T = 0 \ &\Rightarrow \ |\lambda_T| \le \mu\lambda_N \quad \text{(stick)}, \\ \dot g_T < 0 \ &\Rightarrow \ \lambda_T = \mu\lambda_N \quad \text{(negative slip)}, \\ \dot g_T > 0 \ &\Rightarrow \ \lambda_T = -\mu\lambda_N \quad \text{(positive slip)}. \end{aligned} \tag{11}$$

The three different regimes of free-flight, slip and stick are analyzed separately in the following sections, together with the transition conditions from one regime to the others.

3 Free-flight

Free-flight occurs when $g_N > 0$. In this case there is no contact with the moving surface, so that $\lambda_N = \lambda_T = 0$, and there are only the kinematic unknowns $\mathbf{u} = [\varphi,\, y]^T$ (2 mechanical dof), which are determined by solving equations (8) with $\mathbf{f} = \mathbf{0}$. Since $\det \mathbf{M} > 0,\ \forall\, \mathbf{u}$, these equations reduce to

$$\ddot{\mathbf{u}} = \mathbf{M}^{-1}(\mathbf{u})\mathbf{h}(\mathbf{u}, \dot{\mathbf{u}}), \tag{12}$$

and can be easily integrated numerically.

Free-flight occurs as long as $g_N > 0$, a condition that must be verified during the numerical computations. When $g_N = 0$, two situations may occur: (i) $\dot{g}_N = 0$, and (ii) $\dot{g}_N < 0$.

The first case corresponds to the so-called "grazing" [16]. Although it is known that it plays an important role in many bifurcation scenarios, its study is out of the scopes of the present work. However, we insert a warning in the numerical code and stop the computations when a grazing is encountered.

The second case, which is the common one, is considered in the next section.

3.1 Impact

We model the impact according to the Poisson's (impulse) law proposed in [21], which is summarized here and adapted to the present work. A very similar model is discussed in [10], while an energetic restitution law is considered in [17].

Although the impact is assumed to be instantaneous, only in its modelling it is customary to consider that it occurs in an infinitesimal time interval $[t_A, t_E]$, in which two phases are identified: a compression, $t \in [t_A, t_C]$, and an expansion, $t \in [t_C, t_E]$. The compression phase is defined by the condition $\dot{g}_N < 0$, whereas the expansion phase by $\dot{g}_N > 0$. Furthermore, the position $\mathbf{u}$ is assumed to be continuous and constant during the impact, whereas the velocity $\dot{\mathbf{u}}$ has a discontinuity as a consequence of the impulses generated at the impact.

3.1.1 Compression

Integrating equation (8) over the compression interval $[t_A, t_C]$ we obtain

$$\mathbf{M}(\dot{\mathbf{u}}_C - \dot{\mathbf{u}}_A) = \mathbf{F}\mathbf{i}_C, \tag{13}$$

where $\mathbf{i}_C = [\Lambda_{NC}, \Lambda_{TC}]^T = [\int_{t_A}^{t_C} \lambda_N \, dt, \ \int_{t_A}^{t_C} \lambda_T \, dt]^T$ is the vector of the impulses of the vertical and horizontal contact forces. We notice that the integral of $\mathbf{h}$ in (8) vanishes because $\mathbf{u}$ is continuous and the time interval is infinitesimal.

Let $\mathbf{w} = [0, -\dot{s}]^T$, and rewrite $(3)_{2,3}$ in the form:

$$\dot{\mathbf{g}} = \mathbf{F}^T \dot{\mathbf{u}} + \mathbf{w}. \tag{14}$$

By evaluating (14) in t_A and t_C, subtracting these equations, noting that $\mathbf{F}$ depends only on $\mathbf{u}$ and thus it is constant during the impact, we get

$$\dot{\mathbf{g}}_C - \dot{\mathbf{g}}_A = \mathbf{F}^T(\dot{\mathbf{u}}_C - \dot{\mathbf{u}}_A), \tag{15}$$

which, using (13), is written as function of the impulses

$$\dot{\mathbf{g}}_C = \mathbf{G}\mathbf{i}_C + \dot{\mathbf{g}}_A, \tag{16}$$

where $\mathbf{G} = \mathbf{F}^T \mathbf{M}^{-1} \mathbf{F}$. In components (16) reads as

$$\begin{bmatrix} \dot{g}_{NC} \\ \dot{g}_{TC} \end{bmatrix} = \begin{bmatrix} G_{11} & G_{12} \\ G_{21} & G_{22} \end{bmatrix} \begin{bmatrix} \Lambda_{NC} \\ \Lambda_{TC} \end{bmatrix} + \begin{bmatrix} \dot{g}_{NA} \\ \dot{g}_{TA} \end{bmatrix}. \tag{17}$$

The unknowns of the two scalar equations (17) are $\dot{g}_{NC}$, $\dot{g}_{TC}$, Λ_{NC} and Λ_{TC} ($\dot{g}_{NA} < 0$ and $\dot{g}_{TA}$ are known because they are the hitting relative velocities), so that two further equations are required. They are obtained by considering the normal and the tangential behavior in compression.

The phase of compression ends, at $t = t_C$, when the normal relative velocity vanishes,

$$\dot{g}_{NC} = 0. \tag{18}$$

This is the third equation. Since the normal reaction λ_N is always positive, also the impulse is positive,

$$\Lambda_{NC} > 0. \tag{19}$$

As far as the behavior in the tangential direction is concerned, it is assumed that the Coulomb's law (11), which is valid for forces, extends to the impulses (see [21] for more details):

$$\begin{array}{lcll} \dot{g}_{TC} = 0 & \Rightarrow & |\Lambda_{TC}| \leq \mu\Lambda_{NC} & \text{(stick)}, \\ \dot{g}_{TC} < 0 & \Rightarrow & \Lambda_{TC} = \mu\Lambda_{NC} & \text{(negative slip)}, \\ \dot{g}_{TC} > 0 & \Rightarrow & \Lambda_{TC} = -\mu\Lambda_{NC} & \text{(positive slip)}. \end{array} \tag{20}$$

In each of the previous three cases there is an equality, which is the fourth equation, and an inequality, which has to be checked together with (19).

In the numerical simulations we explicitly consider all the three cases. If only one is possible, then the solution is unique, we take the correct values of $\dot{g}_{NC} = 0$, $\dot{g}_{TC}$, Λ_{NC} and Λ_{TC}, and proceed further. If, on the contrary, none or more than one is possible, we encounter a paradox, and, according to what has been said in the Introduction, we terminate the computation.

Finally we note that the behavior in the tangential direction is dissipative, since $\Lambda_{TC} \cdot \dot{g}_{TC} \leq 0$ in any case.

3.1.2 Expansion

Repeating the same reasoning of the compression phase in the infinitesimal interval $[t_C, t_E]$ we obtain ($\mathbf{G}$ is the same of the compression phase):

$$\dot{\mathbf{g}}_E = \mathbf{G}\mathbf{i}_E + \dot{\mathbf{g}}_C. \tag{21}$$

Now $\mathbf{i}_E = [\Lambda_{NE}, \Lambda_{TE}]^T = [\int_{t_C}^{t_E} \lambda_N \, dt, \int_{t_C}^{t_E} \lambda_T \, dt]^T$ is the vector of the impulses in the expansion phase.

Again, two further equations are required to determine the four unknowns $\dot{g}_{NE}$, $\dot{g}_{TE}$, Λ_{NE} and Λ_{TE} ($\dot{g}_{NC} = 0$ and $\dot{g}_{TC}$ have been computed in the compression phase).

The behavior in the normal direction is governed by the Poisson's law, according to which the elastic deformation in compression releases an expansion impulse which is proportional to the impulse at compression:

$$\Lambda_{NE} = \varepsilon_N \Lambda_{NC}. \tag{22}$$

This is the third equation. $\varepsilon_N \geq 0$ is the restitution coefficient, and it is a constitutive parameter of the model which should be determined experimentally.

The relative normal velocity at the end of the expansion must be non-negative, $\dot{g}_{NE} \geq 0$. Indeed, it has been shown in [11] that the mass m_1 always rebound if $\varepsilon_N > 0$, namely

$$\dot{g}_{NE} > 0. \tag{23}$$

The behavior in the tangential direction is similar to that in the compression phase, and it is given by (20) by simply changing the subscript C with E.

Again, in each of the three cases there is an equality, which is the fourth equation, and an inequality, which has to be checked together with (23).

In the numerical simulations we consider all the three cases. If only one is possible, than the solution is unique, we get the corresponding $\dot{g}_{NE}$, $\dot{g}_{TE}$, Λ_{NE} and Λ_{TE}, and proceed further. If, on the contrary, none or more than one is possible, we encounter a paradox and stop the computation.

Remark. In [21] a more involved model is considered, which is aimed at describing also the "superball" effect. See [21] and [11] for more details. In [15] and in [24] a tangential impact is also considered. □

Summarizing, we enter the impact phase knowing the impact position φ_A and $y_A = l\cos(\varphi_A)$, and the velocities $\dot{\varphi}_A$ and $\dot{y}_A$. With these latter we compute $\dot{g}_{NA}$ and $\dot{g}_{TA}$ by $(3)_{2,3}$ and then, following the previous developments, $\dot{g}_{NE}$ and $\dot{g}_{TE}$. Using again $(3)_{2,3}$ we get the initial velocities $\dot{\varphi}_E$ and $\dot{y}_E$ for the subsequent motion, while the continuity of the displacements gives $\varphi_E = \varphi_A$ and $y_E = y_A$.

Note that all these computations are algebraic, and that the (infinitesimal) length of the time interval $[t_A, t_E]$ does not appear explicitly. This confirms that the impact is actually considered instantaneous in this model.

3.2 From free-flight to contact regimes

3.2.1 Infinitely many impacts

As previously said, it has been shown in [11] that $\dot{g}_{NE} > 0$ provided that $\varepsilon_N > 0$. This means that the mass m_1 always bounces, and there is no *generic direct* transition from free-flight to contact regimes. This transition in general occurs *indirectly*. In fact, in certain situations an infinite sequence of impacts occur at times t_i, $i \in \mathbb{N}$, and the impact instants accumulate on a certain $\hat{t}$,

$\lim_{i\to\infty} t_i = \hat{t}$, while the normal impulses tend to zero, $\lim_{i\to\infty} \Lambda_{NC,i} = 0$, as well as the normal relative velocity, $\lim_{i\to\infty} \dot{g}_{NE,i} = 0$.

In the numerical simulations it is not easy to detect the accumulation point $\hat{t}$. We conventionally end the process when the time distance between two consecutive impacts, $|t_{i+1} - t_i|$, is smaller than a given, very small, tolerance.

At the end of this process, which has been studied in detail in [2, 5] where it has been named 'chattering', and in [18] where it has been named 'complete chattering', the motion goes to a contact regime. To decide whether stick or slip is the subsequent motion, we use the exit condition for the impact as the initial conditions for both stick and slip, and immediately check their feasibility (practically, for slip we check if λ_N given by (31) is positive, and for stick we check if λ_T and λ_N computed with the formulas reported in Sect. 5 satisfy $|\lambda_T| < \mu\lambda_N$). If only one is admissible, the motion proceed with that phase, otherwise a paradox is encountered and, as usual, we stop the numerical simulations.

3.2.2 Completely inelastic impact

A different transition from free-flight to contact regimes is obtained in the case of a perfectly plastic impact. This is obtained by setting $\varepsilon_N = 0$, i.e., by assuming that there is no expansion impulse or, alternatively, that all the normal impact energy is dissipated.

In this case the expansion phase disappears, $t_E \equiv t_C$, and the solution is that of the compression phase

$$\dot{g}_{NE} = \dot{g}_{NC} = 0, \quad \dot{g}_{TE} = \dot{g}_{TC}. \tag{24}$$

Remark. The perfectly plastic impact can be seen as the limit of the Poisson's impact law described in the previous sections as $t_C \to t_E$ (see [11] for more details). A perfectly plastic impact is considered in [12]. □

Contrarily to the previous case, here the transition to contact regimes is instantaneous, and does not require any special care in the numerical simulations. Similarly to the previous case, instead, the contact regime following the impact is chosen by checking the feasibility of both slip and stick motions, continuing the computation if only one is possible and stopping it if none or both are possible.

Remark. It is useful to determine the manifold which separates the stick and slip post-impact regions in the phase space. This manifold can be detected by assuming that the stick post-impact condition ($\dot{g}_{TE} = 0$, namely $\dot{g}_{TC} = 0$) and the slip post-impact condition ($\Lambda_{TE} = \mu\Lambda_{NE}$, namely $\Lambda_{TC} = \mu\Lambda_{NC}$) occur simultaneously. With these conditions, from (17) we obtain that $\Lambda_{NC} = -\dot{g}_{NA}/(G_{11} + \mu G_{21})$ and that the equation

$$H(\varphi_A)\dot{g}_{NA}(\varphi_A, \dot{\varphi}_A, \dot{y}_A) = \dot{g}_{TA}(\varphi_A, \dot{\varphi}_A), \quad \text{with } H = \frac{G_{21} + \mu G_{22}}{G_{11} + \mu G_{12}}, \tag{25}$$

must be satisfied by the impact entering variables φ_A, $\dot{\varphi}_A$ and $\dot{y}_A$. Equation (25) is the analytical expression of the searched boundary manifold. Note that in the sub-space (φ,$\dot{\varphi}$), it is a curve parametrized by $\dot{y}_A$. □

4 Slip

Slip is the first of the two contact regimes to be analyzed. Both are characterized by $g_N = 0$ and $\dot{g}_N = 0$, and as far as contact is maintained, also by $\ddot{g}_N = 0$. From these expressions and (3) we obtain

$$y = l\cos\varphi, \quad \dot{y} = -l\dot{\varphi}\sin\varphi, \quad \ddot{y} = -l\dot{\varphi}^2\cos\varphi - l\ddot{\varphi}\sin\varphi, \tag{26}$$

which show how, in these cases, y is no longer an independent variable.

In the case of slip, φ is the unique independent variable (1 dof). To determine the governing equation, we note that if m_1 slides on the moving surface, then $\dot{g}_T \neq 0$, and, from the Coulomb law $(11)_{2,3}$, we have that:

$$\lambda_T = \mu\lambda_N \text{ (if } \dot{g}_T < 0) \text{ or } \lambda_T = -\mu\lambda_N \text{ (if } \dot{g}_T > 0). \tag{27}$$

We write all equations in the present section by supposing $\lambda_T = \mu\lambda_N$; the other case is obtained by changing μ with $-\mu$ (alternatively, we can consider $\lambda_T = -sign(\dot{g}_T)\mu\lambda_N$). By inserting expression (10) in the expression $\lambda_T = \mu\lambda_N$, and using (26), we get (see [12])

$$m(\varphi)\ddot{\varphi} + v(\dot{\varphi}, \varphi) = 0, \tag{28}$$

where

$$\begin{array}{rcl} m(\varphi) & = & (m_1\cos^2\varphi + m_2\sin^2\varphi + \mu m_2\sin\varphi\cos\varphi)l^2, \\ v(\dot{\varphi}, \varphi) & = & a_1(\varphi)\dot{\varphi}^2 + a_2(\varphi)\dot{\varphi} + a_3(\varphi), \end{array} \tag{29}$$

and

$$\begin{aligned} a_1(\varphi) &= [(m_2 - m_1)\sin\varphi\cos\varphi + \mu m_2\cos^2\varphi]l^2, \\ a_2(\varphi) &= \mu c_v l^2\cos\varphi\sin\varphi + c_v l^2\sin^2\varphi + c_\varphi, \\ a_3(\varphi) &= k_\varphi(\varphi-\varphi_0) - k_v l^2\sin\varphi\cos\varphi - \mu k_v l^2\cos^2\varphi + k_v y_0 l\sin\varphi + \\ &\quad + \mu k_v y_0 l\cos\varphi - (m_1+m_2)(\sin\varphi + \mu\cos\varphi)gl + m_1 gl\sin\varphi. \end{aligned} \tag{30}$$

Equation (28) is integrated numerically. Once the solution $\varphi(t)$ is determined, the normal reaction λ_N is evaluated by substituting (26) and (28) in $(10)_1$:

$$\lambda_N = m_2 l\left(\frac{v(\dot\varphi,\varphi)}{m(\varphi)}\sin\varphi - \dot\varphi^2\cos\varphi\right) - c_v l\dot\varphi\sin\varphi + k_v l\cos\varphi - k_v y_0 + (m_1+m_2)g. \tag{31}$$

Slip occurs if $m(\varphi) > 0$, $\dot g_T \neq 0$ and $\lambda_N > 0$, three conditions that must be verified during the numerical computations. When $m(\varphi) \leq 0$, the Painlevé paradox occurs (Sect. 4.2); when $\dot g_T = 0$ we have a transition to stick or to inverted slip (Sect. 4.3); when λ_N vanishes we have a transition to free-flight (Sect. 4.4). Before analyzing these cases, however, we discuss the equilibrium points in the slip regime.

4.1 Equilibrium points and their stability

Equilibrium positions $\varphi = \bar\varphi$ and $y = l\cos\bar\varphi$ of the system of Fig. 1 are possible if the surface velocity does not change sign, e.g., if it is constant. They experience only the slip regime, so that, from (28), they are the solutions of $a_3(\bar\varphi) = 0$.

The determination of the stability of these solutions is a difficult problem. In fact, they are (equilibrium) solution of the whole 2 dof system, so that the computation of the eigenvalues of the whole 4×4 Jacobian matrix is required. Moreover, the problem is even more complex, because we are dealing with a non-smooth unilaterally constrained motion, so that classical analysis may fail [14].

As a consequence of the previous observation, and because it is sufficient for the purposes of the present work, we study only the stability *on* the constrained manifold $g_N = 0$, i.e., we investigate only the stability of the equilibrium of the equation (28), neglecting the out-of-manifold dimensions. Thus, we only obtain necessary conditions for stability (or sufficient

conditions for instability). Fortunately, we will show with some numerical simulations (Sect. 6.1) that, in some cases, this analysis captures exactly the bifurcation point where stability is lost.

The Jacobian matrix of the system (28) at equilibrium is given by (see [11] for more details)

$$\mathbf{J} = \frac{-1}{m(\bar{\varphi})} \begin{bmatrix} 0 & -m(\bar{\varphi}) \\ a_3'(\bar{\varphi}) & a_2(\bar{\varphi}) \end{bmatrix}. \tag{32}$$

Let $\lambda_1(\bar{\varphi})$ and $\lambda_2(\bar{\varphi})$ be the eigenvalues of (32). The equilibrium is stable if $\mathrm{Re}(\lambda_1) < 0$ and $\mathrm{Re}(\lambda_2) < 0$.

The equilibrium reaches a saddle-node bifurcation if one of the eigenvalues is equal to zero. This occurs when $a_3'(\bar{\varphi}) = 0$, i.e., when $a_3(\varphi)$ has a double zero. The bifurcation is instead a Hopf when $\mathrm{Re}(\lambda_i) = 0$, $\mathrm{Im}(\lambda_i) \neq 0$, $i = 1, 2$. This occurs when $a_2(\bar{\varphi}) = 0$ and $a_3'(\bar{\varphi}) > 0$. Note that if $c_\varphi > (c_v l^2/2)(\sqrt{1+\mu^2} - 1)$ we have that $a_2(\varphi)$ is always different from zero, so that Hopf bifurcation is not possible.

4.2 Painlevé paradox

In (28), $m(\varphi)$ vanishes when

$$\varphi = \arctan[\frac{\mu}{2}(-1 \pm \sqrt{1 - \frac{4}{\mu^2}\frac{m_1}{m_2}})], \tag{33}$$

which is a real number only if [12]

$$\mu > \mu_{crit} = 2\sqrt{\frac{m_1}{m_2}}. \tag{34}$$

If $\mu < \mu_{crit}$ the mass term $m(\varphi)$ never vanishes, whereas for μ above μ_{crit} it is possible that the term $m(\varphi)$ vanishes. When $m(\varphi) = 0$, two cases are possible:

(*i*) $v(\dot{\varphi}, \varphi) \neq 0$; then $\ddot{\varphi} \to \infty$ and the solution no longer exist;

(*ii*) $v(\dot{\varphi}, \varphi) = 0$, and the solution is not unique in principle.

This is a manifestation of the Painlevé paradox, which can be better studied by reformulating the problem in the form of a linear complementary problem (LCP). This has been previously investigated in [12] and [21], and their main results are summarized in the next subsection.

4.2.1 The Linear Complementary Problem

Let us consider the expression $(3)_4$ of $\ddot{g}_N$. If we (i) evaluate $\ddot{\varphi}$ and $\ddot{y}$ from the equation of motion (8), (ii) use the condition of slip $\lambda_T = \mu\lambda_N$ (we suppose positive sliding), and (iii) use the conditions of contact $g_N = \dot{g}_N = 0$ (i.e., $y = l\cos\varphi$ and $\dot{y} = -l\dot{\varphi}\sin\varphi$), then we have [12]

$$\ddot{g}_N = A(\varphi)\lambda_N + b(\dot{\varphi}, \varphi), \tag{35}$$

where

$$\begin{aligned} A(\varphi) &= \frac{1}{(m_1\cos^2\varphi + m_2)}\frac{m_2}{m_1}(\frac{m_1}{m_2}\cos^2\varphi + \sin^2\varphi + \mu\sin\varphi\cos\varphi) \\ b(\dot{\varphi}, \varphi) &= \frac{1}{l(m_1\cos^2\varphi + m_2)}\{m_2 l^2\cos\varphi\dot{\varphi}^2 + [-c_\varphi\frac{m_2}{m_1}\sin\varphi + c_v l^2\sin\varphi\cos^2\varphi]\dot{\varphi} + \\ &\quad + [-k_v l^2\cos^3\varphi - k_\varphi\frac{m_2}{m_1}(\varphi - \varphi_0)\sin\varphi + lk_v y_0\cos^2\varphi]\} - g. \end{aligned} \tag{36}$$

In the case of negative sliding, $\lambda_T = -\mu\lambda_N$ and in (36) μ has to be replaced with $-\mu$.

When the mass is in contact with the moving surface, the force λ_N can be greater than zero and $\ddot{g}_N$ must be zero, or $\ddot{g}_N$ can be greater than zero and λ_N must be zero. We thus obtain the linear complementary problem (35) and

$$\ddot{g}_N \geq 0,\ \lambda_N \geq 0,\ \ddot{g}_N \cdot \lambda_N = 0. \tag{37}$$

The following cases are possible:

- $A > 0$ (1 solution)
  1. $b > 0 \rightarrow \lambda_N = 0$, $\ddot{g}_N = b$ (free-flight);
  2. $b < 0 \rightarrow \lambda_N = -b/A$, $\ddot{g}_N = 0$ (slip);
- $A < 0$ (2 solutions or no solutions)
  1. $b > 0 \rightarrow \lambda_N = 0$, $\ddot{g}_N = b$ (free-flight), or $\lambda_N = -b/A$, $\ddot{g}_N = 0$ (slip)
  2. $b < 0 \rightarrow$ no solutions.

We note that $A(\varphi) = m(\varphi)/[m_1(m_2 + m_1\cos^2\varphi)]$, so that $A(\varphi) = 0$ if and only if $m(\varphi) = 0$. Moreover, when the Painlevé paradox occurs, $A(\varphi) < 0$ [21], also the mass-like term $m(\varphi)$ becomes negative.

4.3 From slip to stick or to inverted slip

The motion passes from slip to stick or to inverted slip when $\dot{g}_T = 0$. This occurs at a certain $\hat{\varphi}$, and the associated velocity and acceleration are, respectively,

$$\hat{\dot{\varphi}} = \frac{\dot{s}}{l\cos(\hat{\varphi})}, \quad \hat{\ddot{\varphi}} = -\frac{v(\hat{\dot{\varphi}}, \hat{\varphi})}{m(\hat{\varphi})}. \tag{38}$$

They depend on the transition position $\hat{\varphi}$ only.

To decide the next regime, we check independently the admissibility of impending stick or inverted slip.

Stick after slip

To verify if stick follows slip, we compute the tangential λ_T^+ and the normal λ_N^+ contact forces at the beginning of the hypothetical subsequent stick regime. They are given by inserting the expressions (26) of y, $\dot{y}$ and $\ddot{y}$ in (10), and by using in the resulting formulas $\varphi = \hat{\varphi}$,

$$\dot{\varphi} = \frac{\dot{s}}{l\cos\hat{\varphi}}, \quad \ddot{\varphi} = \frac{\ddot{s}}{l\cos\hat{\varphi}} + \frac{(\dot{s})^2\sin\hat{\varphi}}{l^2\cos^3\hat{\varphi}} \tag{39}$$

(these are the equations of the stick regime, which will be obtained in the next Section).

Stick after the transition is possible if $|\lambda_T^+| \leq \mu\lambda_N^+$.

Inverted slip

To check whether inverted slip might occur at $\dot{g}_T = 0$, we compute the tangential relative acceleration at the end of the finishing slip regime

$$\ddot{g}_T^- = l\hat{\ddot{\varphi}}\cos\hat{\varphi} - l\hat{\dot{\varphi}}^2\sin\hat{\varphi} - \ddot{s}, \tag{40}$$

where $\hat{\dot{\varphi}}$ and $\hat{\ddot{\varphi}}$ are given by (38), so that (40) is a function of $\hat{\varphi}$ only.

Then, we compute the tangential relative acceleration at the beginning of the hypothetical next slip regime, $\ddot{g}_T^+$. It is given by (40) by simply changing the sign of μ in the expression $v(\hat{\dot{\varphi}}, \hat{\varphi})$ appearing in $(38)_2$.

Inverted slip is possible if the relative velocity $\dot{g}_T$ continuously changes sign across the point where $\dot{g}_T = 0$. This occurs when $\ddot{g}_T^-$ and $\ddot{g}_T^+$ have the same sign, i.e., $\ddot{g}_T^+ \cdot \ddot{g}_T^- > 0$.

Transition at the end of slip

Now that we have (independently) computed $\ddot{g}_T^+$, $\ddot{g}_T^-$, λ_T^+ and λ_T^- we are in position to determine the transition at the end of the slip regime. Only four generic cases are possible:
(i) $|\lambda_T^+| \leq \mu\lambda_N^+$ and $\ddot{g}_T^+ \cdot \ddot{g}_T^- < 0 \Rightarrow$ we switch to stick, which is the only possible subsequent motion;
(ii) $|\lambda_T^+| \geq \mu\lambda_N^+$ and $\ddot{g}_T^+ \cdot \ddot{g}_T^- > 0 \Rightarrow$ we switch to inverted slip, which is the unique possibility;
(iii) $|\lambda_T^+| > \mu\lambda_N^+$ and $\ddot{g}_T^+ \cdot \ddot{g}_T^- < 0 \Rightarrow$ no solution exists.
(iv) $|\lambda_T^+| \leq \mu\lambda_N^+$ and $\ddot{g}_T^+ \cdot \ddot{g}_T^- > 0 \Rightarrow$ two solutions exist;

Note that cases (iii) and (iv) highlight the possible presence of another paradox. In these cases the numerical simulations are interrupted, as well as in the non generic situation $\ddot{g}_T^+ \cdot \ddot{g}_T^- = 0$ which is similar to grazing.

4.4 From slip to free-flight

The motion moves from slip to free-flight when $\lambda_N = 0$, which, by (35), is equivalent to $b = 0$ ($\ddot{g}_N = 0$ because we are in a slip regime, although at the end of it). Consequently, in the phase space (φ,$\dot{\varphi}$), the curve implicitly defined by $b(\dot{\varphi}, \varphi) = 0$ is the locus of points of slip to free-flight transition.

Note that during the transition the function b behaves as follows: $b < 0$ (slip) $\Rightarrow b = 0$ (transition) $\Rightarrow b > 0$ (free-flight).

Let $\hat{\varphi}$ and $\hat{\dot{\varphi}}$ be the angle and the velocity at the instant of time for which $\lambda_N = 0$. The initial conditions for the subsequent free-flight regime are: $\varphi = \hat{\varphi}$, $\dot{\varphi} = \hat{\dot{\varphi}}$, $y = l\cos\hat{\varphi}$ and $\dot{y} = -l\hat{\dot{\varphi}}\sin\hat{\varphi}$.

5 Stick

In the stick case the mass m_1 adheres to the moving surface, so that the motion has no dof. In addition to (26), we also have $\dot{g}_T = \ddot{g}_T = 0$, which yields

$$\dot{\varphi} = \frac{\dot{s}}{l\cos\varphi}, \quad \ddot{\varphi} = \frac{\ddot{s}}{l\cos\varphi} + \frac{(\dot{s})^2\sin\varphi}{l^2\cos^3\varphi}. \tag{41}$$

Integrating $\dot{g}_T = 0$ we obtain

$$\varphi(t) = \arcsin[\,\sin\hat{\varphi} + \frac{1}{l}\int_{\hat{t}}^{t} \dot{s}(\tau)d\tau\,], \tag{42}$$

which gives the angle $\varphi(t)$ as a function of the driving velocity. In (42) $\hat{\varphi}$ is the angle and $\hat{t}$ the time at the beginning of the considered stick regime.

If we substitute (41)-(42) in (26), and the result in (10), we obtain the reactive forces λ_N and λ_T as a function of $\dot{s}$ and $\ddot{s}$.

Note that in the space $(\varphi, \dot{\varphi})$ the stick motions belong to the curve defined by $(41)_1$, which is explicitly independent on time only in the case of constant surface velocity.

Stick occurs as far as $|\lambda_T| < \mu\lambda_N$ and $\lambda_N > 0$. When $|\lambda_T| = \mu\lambda_N$ we have a transition to slip (Sect. 5.1); when $\lambda_N = 0$ we have a transition to free-flight (Sect. 5.2).

5.1 From stick to slip

A stick phase passes to slip when $\lambda_T = \mu\lambda_N$ (negative slip, $\dot{g}_T < 0$) or $\lambda_T = -\mu\lambda_N$, (positive slip, $\dot{g}_T > 0$).

Of course, we have to check that incipient slip is possible. λ_N remained positive during all the stick phase (otherwise there would be transition to free-flight), so it is positive also at the transition and just after. The relative tangential velocity $\dot{g}_T$ is zero up to the transition and then continuously will become different from zero. The only meaningful check is then on the sign of $m(\varphi)$ (and thus on the sign of $A(\varphi)$), which may turn to a negative value during the stick phase.

If $m(\varphi)$ (and $A(\varphi)$) is positive, according to the contents of Sect. 4.2.1 the solution is unique and we proceed further. If $m(\varphi) < 0$ (and $A(\varphi) < 0$) the Painlevé paradox occurs, and we have to consider the sign of b. If b is negative there is no solution, and the computations stop. If, on the other hand, $b > 0$ we can have slip or free-flight after transition (see Sect. 4.2.1).

Since we do not accept negative values of the mass-like term $m(\varphi)$, in this case we proceed to free-flight. In this transition λ_N jumps instantaneously from a positive value to zero. This choice is supported by the results of [12], where it is proved (Lemma 5.3), for a Simplified Frictional Impact Oscillator, that the unique transition is from stick to free-flight.

5.2 From stick to free-flight

The transition from stick to free-flight apparently does not differ from the slip to free-flight transition which has been studied in Sect. 4.4. A difference

instead occurs. In fact, when $\lambda_N = 0$ also $\lambda_T = 0$, so that both the conditions $\lambda_N = 0$ and $|\lambda_T| = \mu\lambda_N$ are satisfied simultaneously. Thus, in principle, both the transitions to free-flight and to slip are possible. As usual, we proceed if only one is possible, and stop if none or both are feasible.

It is important to remark that, in some sense, this case constitutes a pathological situation. In fact, it requires that, during the stick phase, the point (λ_N, λ_T) in the plane of the contact forces reaches the vertex of the friction cone with no previous intersection with the cone itself (otherwise a transition to slip will happen earlier), which is not a generic situation. To support this conclusion, we observe that in the numerical simulations of Sect. 6 we never encounter a stick to free-flight transition.

6 Numerical simulations

In this section two series of numerical simulations are reported.

In the first we assume a constant surface velocity and we analyze the influence of the frictional coefficient μ and of the angle of the unstressed configuration φ_0 on the dynamics. Different values of the restitution coefficient ε_N and of the ratio m_1/k_φ are considered.

In the second we consider a sinusoidal surface velocity. Preliminary tests are performed to investigate the hopping phenomenon, which usually takes place when φ and $\dot{s}$ have opposite signs, i.e. when the motion of the surface compresses the vertical spring. This phenomenon is unwanted in many practical applications. If, for example, we consider the motion of windscreen wipers, the bounces of the blade on the glass produce undesired noise and marks which reduce the visibility. In the case of robotic fingers, the hopping reduces the displacement precision and stresses the system by means of dangerous impulsive forces. We analyze the influence of the friction and of the unstressed springs configurations on the hopping motion.

6.1 Constant surface velocity

We set $l = 1$ m, $m_2 = 1$ kg, $k_y = 100$ N/m, $c_y = 10$ N/(ms), $c_\varphi = 0$, $y_0 = 1$ m, and $\dot{s} = -1$ m/s, and consider both an elasto-plastic impact law, assuming $\varepsilon_N = 0.2$, and a perfectly plastic law as in [12], setting $\varepsilon_N = 0$. The friction coefficient μ and the angle of the unstressed configuration φ_0 of

the rotational spring play the role of governing parameters. Two simulations are performed with different values of the ratio m_1/k_φ.

6.1.1 Simulation 1

We consider the values $m_1 = 0.1$ kg and $k_\varphi = 100$ Nm. For $\varepsilon_N = 0$ (perfectly plastic impact), the chosen parameters coincide with those used in the simulations of [12], which are used as a benchmark to check the accuracy of our numerical code. Then, they are compared with the results obtained with $\varepsilon_N = 0.2$ in order to have some hints on the differences induced by different impact laws.

Bifurcation diagrams for varying μ

We fix $\varphi_0 = \pi/8$. The influence of the friction coefficient μ on the motion is described by the bifurcation diagrams of Fig. 2. The maximum angular velocity $\dot{\varphi}$ of the motion is plotted versus μ.

For small values of μ we observe only an equilibrium branch, which corresponds to that analytically computed in Sect. 4.1. As it is in a slip mode, no impacts are involved and thus the diagrams for $\varepsilon_N = 0$ and $\varepsilon_N = 0.2$ coincide. Furthermore, the equilibrium branch is horizontal, being $\dot{\varphi}$ constantly equal to zero, but the equilibrium configurations actually depend on μ: φ increases as μ increases, according to the equilibrium equation $a_3(\varphi) = 0$, see Sect. 4.1.

By increasing μ, the equilibrium undergoes an Hopf bifurcation at $\mu = 0.40977$, after which a periodic oscillation in slip mode appears. This bifurcation occurs within the slip mode, so that the bifurcation point coincides with that analytically computed in Sect. 4.1. Furthermore, as the system remains in a slip mode, the diagrams for $\varepsilon_N = 0$ and $\varepsilon_N = 0.2$ still coincide. The equilibrium point $(\varphi = 0.392, \dot{\varphi} = 0)$ for $\mu = 0.3$ and the periodic oscillation for $\mu = 0.4098$ are reported in Fig. 3.

The slip periodic branch exists only in a narrow range of values of μ. In fact, at $\mu = 0.40983$ it suddenly disappears and the dynamics jump on another branch of solutions, which exists also for smaller values of μ. This branch involves free-flight and impacts, and thus the path for $\varepsilon_N = 0$ is different from that for $\varepsilon_N = 0.2$. The two branches differ even for the starting point, which corresponds to $\mu \simeq 0.3882$ for $\varepsilon_N = 0.2$ and to $\mu \simeq 0.3896$ for $\varepsilon_N = 0$.

It is worth to note how the transition from contact motions to detached

motions occurs through a hysteretic loop (see Fig. 2(b)), which is defined by the region of coexistence of the two solutions.

In the case $\varepsilon_N = 0.2$, the detached motion consists of a sequence of periodic bounces of m_1 on the moving surface. Its orbit is denoted as 'bouncing' in Fig. 3(a), while a time history is reported in Fig. 4(a). It has a single jump of $\dot{\varphi}$, corresponding to the impact. The periodic motion does not depend on μ since the friction enters only at the impact instants (a numerable set of instants) and do not affect significantly the dynamics in this case. As a result, the periodic branch is horizontal.

In the case $\varepsilon_N = 0$ the motion consists of a sequence of free flight-stick-slip phases which repeat periodically, this occurring in the range $0.3979 < \mu < 0.6450$. The phase portrait for $\mu = 0.6$ is drawn in Fig. 3(b), and the corresponding time history is reported in Fig. 4(b). After the free-flight phase, at the impact the orbit jumps to the curve $\dot{g}_T = 0$ (equation $(41)_1$), and the motion continues in stick mode. There is a transition to slip mode when the stick curve intersects the friction cone ($\lambda_T = -\mu\lambda_N$), and then a transition from slip to free-flight occurs when the orbit intersects the curve $b = 0$ (b is defined in $(36)_2$), as described in Sect. 4.2.1.

Near the bifurcation point $\mu = 0.3896$ (see Fig. 2(c) for an enlargement of the corresponding bifurcation branch) the motion has the following behavior. At $\mu = 0.3979$, the periodic motion passes from free flight-stick-slip ($\mu > 0.3979$, Fig. 3(b)) to free flight-slip-stick-slip ($\mu < 0.3979$, Fig. 5(b)), i.e., the post-impact phase passes from stick to slip. The phase portrait at this transition is represented in Fig. 5(a), where we note that the impacting values φ_A, $\dot{\varphi}_A$ and $\dot{y}_A$ satisfy equation (25) $H\dot{g}_{NA} = \dot{g}_{TA}$.

As μ decreases in the range $0.3896 < \mu < 0.3979$, the stick phase reduces and the post-impact slip phase increases. At the bifurcation point $\mu \simeq 0.3896$, the stick phase disappears and the two slip parts of the orbit join at the point of intersection between the friction cone and the curve $\dot{g}_T = 0$ (see Fig. 5(c)). This bifurcation looks to be quite complex, and it is still subject to further investigation, but, in any case, after that the motion jumps to the equilibrium branch $\dot{\varphi} = 0$.

When $\mu > 0.645$ the periodic motion loses the slip phase (see the phase portrait for $\mu = 0.8$ in Fig. 3(b)). In this case $A < 0$ (A is defined in $(36)_1$), and the Painlevé paradox occurs at the end of the stick phase, when $\lambda_T = -\mu\lambda_N$. Since $b > 0$ at this point, both free-flight and slip would be possible (see Sect. 4.2.1), but the negative value of the mass-like term $m(\varphi)$ rules out the slip mode and the motion goes in free-flight. However, at the

transition instant from stick to free-flight, the normal reaction λ_N jumps from a positive value to zero. This discontinuity has no mechanical justification, and likely disappears if more sophisticated impact laws are considered.

The loss of the slip phase at $\mu = 0.645$ is evidenced by a non-smooth point in the bifurcation diagram of Fig. 2(a).

A comparison of the plastic and of the elasto-plastic impact cases for fixed values of μ is reported in Figs. 3 and 4. In particular, comparing the time histories in Fig. 4, we notice that the motions for $\varepsilon_N = 0$ and $\varepsilon_N = 0.2$ have practically the same period.

Bifurcation diagrams for varying φ_0

We now fix $\mu = 0.4$ and vary φ_0 in the interval $(0, \pi/5)$. The bifurcation diagrams are represented in Fig. 6. The solid and dashed line curves correspond to the case $\varepsilon_N = 0.2$ and $\varepsilon_N = 0$, respectively. For $\varphi_0 < 0.223$, the mass m_1 never detaches from the belt. An equilibrium branch in slip exists up to $\varphi_0 = 0.044$, and a stick-slip periodic branch is found in the interval $0.044 < \varphi_0 < 0.223$. Within the stick-slip interval, as φ_0 increases, the stick phase increases (see the phase portraits of Fig. 7). At $\varphi_0 = 0.223$ the orbit becomes tangent to the curve $b = 0$ and the free-flight phase enters the motion. For $\varphi_0 > 0.223$ the diagrams corresponding to $\varepsilon_N = 0$ and $\varepsilon_N = 0.2$ do not coincide, despite their closeness up to $\varphi_0 \simeq 0.36$. We consider separately the two cases.

When $\varepsilon_N = 0$ (dashed line in Fig. 6), the system exhibits a periodic motion of the stick-slip-free flight-slip type in the interval $0.223 < \varphi_0 < 0.387$ (see the orbit for $\varphi_0 = 0.350$ in Fig. 8(a)). In this range the post-impact slip phase reduces as φ_0 increases, and at $\varphi_0 = 0.387$ the post-impact regime passes from slip to stick, as confirmed by the fact that the starting impact point $(\varphi_A, \dot{\varphi}_A, \dot{y}_A)$ satisfies equation (25) $H\dot{g}_{NA} = \dot{g}_{TA}$ (this can be clearly seen in Fig. 8(b)).

In the interval $0.387 < \varphi_0 < 0.413$, the periodic motion is stick-slip-free flight. The stick phase reduces as φ_0 increases and at $\varphi_0 = 0.413$ it vanishes. The orbit at this transition point is represented in Fig. 8(c).

Looking to the enlargement of Fig. 8(c), we notice that the impact point $(\varphi_A, \dot{\varphi}_A)$ does not belong to the curve $H\dot{g}_{NA} = \dot{g}_{TA}$, even if the post-impact motion passes from stick to slip. The reason is that the impact problem is solved by a stick solution, i.e., $\dot{g}_{NE} = \dot{g}_{TE} = 0$ and the impulses Λ_{NE} and Λ_{TE}, evaluated by (17), satisfy the inequality $|\Lambda_{TE}| \leq \mu\Lambda_{NE}$. But the tangential and normal forces at the instant $t = t_E$ (impact end) are

such that $|\lambda_T(t_E)| > \mu\lambda_N(t_E)$. As a result, the stick mode cannot start, and only slip motion is allowed with the initial conditions $\varphi = \varphi_A$ and $\dot{\varphi} = \dot{s}/(l\cos\varphi_A)$. The slip mode starts with null relative tangential velocity. The absurd condition $|\lambda_T(t_E)| > \mu\lambda_N(t_E)$, which holds only at the initial instant of the slip post-impact phase, is due to the fact that, at impact, the Coulomb's law is extended to impulses and thus averaged forces are evaluated instead of punctual ones. This is a well known feature of the considered model [21].

In the range $0.413 < \varphi_0 < 0.429$, the motion has the slip and free-flight phases. Within a period, the duration of the slip phase reduces as φ_0 increases, and at $\varphi_0 = 0.429$ it vanishes (see Fig. 8(d)). At this point the orbit is all in free-flight regime, but an impact occurs. The solution of the impact law is a slip point, which belongs to the curve $b = 0$. Thus, after the impact, the motion would continue in slip mode, however it cannot since the orbit enters the region $b > 0$, where only the free-flight regime satisfies the complementary problem (37). As a result a post-impact motion does not exist and the bifurcation branch interrupts. This phenomenon is a consequence of the plastic impact assumption $\varepsilon_N = 0$. In fact, it will no longer exist in the elasto-plastic case $\varepsilon_N = 0.2$ analyzed below.

For $\varphi_0 > 0.429$ only an equilibrium branch survives. The equilibrium is in slip mode for $0.429 < \varphi_0 < 0.478$ and in free-flight mode for $\varphi_0 > 0.478$. The stable equilibrium branch starts at $\varphi_0 = 0.383$. In the range $0.383 < \varphi_0 < 0.413$ the periodic and equilibrium branches coexist (hysteretic behavior).

Now we consider the case $\varepsilon_N = 0.2$. Since for $\varphi_0 < 0.223$ the mass m_1 never detaches from the belt, in this range the motion corresponds to that of the case $\varepsilon_N = 0$. In the interval $0.223 < \varphi_0 < 0.330$ the bifurcation curves of the cases $\varepsilon_N = 0.2$ and $\varepsilon_N = 0$ practically coincides. In the case of elasto-plastic impact, the transition from free-flight to slip occurs through a 'chattering' phenomenon (see Sect 3.2.1). Actually, only the first bounces can be seen in Fig. 9(a), due to the graphical resolution. The bifurcation diagram almost overlaps with that characterized by $\varepsilon_N = 0$ since this phenomenon practically does not modify the values $\dot{\varphi}_{max}$ of the orbits.

At $\varphi_0 = 0.330$, the post-impact slip phase vanishes (the corresponding orbit is represented in Fig. 9(b)). We notice that the same bifurcation point for the case $\varepsilon_N = 0$ is $\varphi_0 = 0.387$. In the range $0.330 < \varphi_0 < 0.365$ the periodic motion is of the type slip-free flight-stick. The stick phase reduces up to vanish at the point $\varphi_0 = 0.365$ (see the orbit in Fig. 9(c)). For

$\varphi_0 = 0.365$ the 'chattering' finishes at the point of intersection between the friction cone and the curve $\dot{g}_T = 0$. The corresponding bifurcation point for the case $\varepsilon_N = 0$ is $\varphi_0 = 0.413$. The slip phase vanishes at $\varphi_0 = 0.374$ (see the phase portrait in Fig. 9(d)), and only the free-flight regime remains, with bounces between free-flight phases.

We remind that in the case $\varepsilon_N = 0$ orbits with only free-flight are impossible, and the bifurcation branch interrupts where they should appear (at $\varphi_0 = 0.429$ in that case); here, on the contrary, we have shown that this kind of motion exists. More precisely, in the range $0.374 < \varphi_0 < 0.386$ the solution consists of chaotic bounces (see Fig. 9(e)) or periodic bounces of period $n > 1$ (see Fig. 9(f) for a period 3 motion). The bouncing becomes of period 1 for $0.386 < \varphi_0 < 0.581$. The value of $\dot{\varphi}_{max}$ rapidly increases, as the bounces rapidly increase their amplitudes. The phase portrait for $\varphi_0 = 0.5$ is represented in Fig. 9(g). The periodic branch ends at $\varphi_0 = 0.581$ and, for $\varphi_0 > 0.581$, only the equilibrium branch in free-flight mode survives.

6.1.2 Simulation 2

We now assume $m_1 = 0.4$ kg and $k_\varphi = 25$ Nm, a case in which the geometrical non-linearity plays a more important role on the dynamics.

Bifurcation diagrams for varying μ

We fix $\varphi_0 = \pi/8$. The bifurcation diagrams for varying μ are reported in Fig. 10. In this case, the diagrams obtained with $\varepsilon_N = 0.2$ and $\varepsilon_N = 0$ *practically* coincide, also in the regions where there is free-flight. The bifurcation curve is constituted by four branches related to four different dynamical behaviors. The branch $\mu < 0.353$ is an equilibrium one. The next three branches correspond to periodic motions: for $0.353 < \mu < 0.360$ the motion is an oscillation in slip mode, for $0.360 < \mu < 0.453$ the periodic oscillation involves also the stick mode, and for $\mu > 0.453$ a more complex free flight-slip-stick-slip motion takes place. In Fig. 10(b) the bifurcation diagram is enlarged in correspondence of the slip oscillating branch. The transition from equilibrium to slip is a Hopf bifurcation occurring at $\mu = 0.353$, a value which coincides with that analytically evaluated in Sect. 4.1.

The orbits in the $(\varphi,\dot{\varphi})$ phase space are reported in Fig. 11 for different values of μ, where we observe that the larger is μ the larger is the diameter of the orbits. The bifurcation values $\mu = 0.360$ and $\mu = 0.453$ correspond to orbits which are tangent to the curves $\dot{g}_T = 0$ (appearance of a stick phase)

and $b = 0$ (appearance of free-flight), respectively.

The motion experiences impacts only for $\mu > 0.453$, and, as a result, only in this region the periodic motion depends on the impact law. Fig. 12 shows the orbits and the time histories of the m_1 vertical displacement for $\mu = 0.49$, for both $\varepsilon_N = 0.2$ and $\varepsilon_N = 0$. In the case $\varepsilon = 0.2$, the solution goes from free-flight to slip through a cascade of accumulating impacts. On the contrary, in the case $\varepsilon_N = 0$, a single impact occurs between free-flight and slip. As shown in Fig. 12 the two orbits differ only in correspondence of the impacts and in the successive slip phase, and they practically coincide in the remaining part. This explains why the bifurcation diagrams for $\varepsilon_N = 0.2$ and $\varepsilon_N = 0$ appear to coincide also when $\mu > 0.453$.

Bifurcation diagrams for varying φ_0

We now fix $\mu = 0.4$ and vary φ_0. The bifurcation diagrams are represented in Fig. 13(a). Since the mass m_1 never detaches from the belt, the diagrams for $\varepsilon_N = 0$ and $\varepsilon_N = 0.2$ coincide. For $\varphi_0 < 0.225$ and $\varphi_0 > 0.442$ the system stays in equilibrium in slip mode. For $0.225 < \varphi_0 < 0.434$ the motion is periodic of the type stick-slip (see Fig. 13(b) for the orbit at $\varphi_0 = 0.4$), and for $0.434 < \varphi_0 < 0.442$ the motion becomes periodic in slip mode. The orbit detaches from the curve $\dot{g}_T = 0$, as shown in Fig. 13(c).

6.2 Surface moving with harmonic velocity

In this subsection we assume a harmonic velocity for the moving surface:

$$\dot{s}(t) = A \sin(\frac{2\pi}{T} t), \tag{43}$$

and assign the values $A = 1$ m/s and $T = 4$ s. All the other data are the same as in Simulation 1. In these preliminary tests we just vary the values of some parameters to see their effect on the dynamics. In particular, we analyze the influence of the parameters μ, φ_0 and y_0, focusing on the hopping phenomenon.

Influence of μ

We fix $\varphi_0 = \pi/8$ and $y_0 = 1$ m, and analyze the influence of the frictional coefficient μ. Varying the value of μ, it is found that mass m_1 never detaches from the belt if $\mu < 0.414$. The orbit in the $(\varphi,\dot{\varphi})$ space and the horizontal displacement of m_1 during a period T are plotted in Fig 14(a) for $\mu = 0.4$.

The mass m_1 mainly slips on the moving surface and sticks only when $\dot{s}$ changes sign. For $\dot{s} < 0$ the motion is an oscillation which asymptotically tends toward the point $\varphi \simeq 0.388$, while, for $\dot{s} > 0$, the oscillation quickly approaches the point $\varphi \simeq 0.409$. The asymmetry of the motion with respect to $\varphi = \dot{\varphi} = 0$ is due to the non null unstressed configuration of the rotational spring ($\varphi_0 = \pi/8$).

For $\mu > 0.414$, bounces take place in the dynamics. As shown in Fig. 14(b) for $\mu = 0.5$, the hopping occurs when $\dot{s} < 0$, and the motion is essentially in free-flight with short slip periods. When $\dot{s} > 0$, the motion is mainly an oscillation in slip mode. Stick mode happens in a time interval during which $\dot{s}$ changes sign.

The motions in the cases of elasto-plastic and perfectly plastic impact models are compared in Fig. 15 for $\mu = 1$. In both cases bounces occur in the half period $\dot{s} < 0$ and oscillations in slip mode take place when $\dot{s} > 0$. When $\varepsilon_N = 0$, stick phases are interposed within the free-flight phases. Looking at the time history of the vertical position x_2 of m_1 in the right part of Fig. 15, we notice that, in the case $\varepsilon_N = 0.2$, the first bounce in the second half period is the highest. Such a bounce is preceded by the stick phase which pumps potential energy in the system, later transformed into (released) kinematic energy during the subsequent free-flight phase. We notice that also the last bounce within the period, preceded by a stick phase, reaches a remarkable height. In the case $\varepsilon_N = 0$, the bounces first increase and then decrease their height. The highest bounce happens when $\dot{s} \simeq -1$ (minimum value). In this case the amount of potential energy pumped in the system during the stick phases seems to be proportional to $|\dot{s}|$.

These simulations reveal the well known dependence of the hopping on the friction. A large value of the friction coefficient facilitates the hopping phenomenon. In fact, according to common sense, we know that, in the case of a windscreen wiper, the hopping occurs when the glass is dirty and dry, i.e., when μ has a large value.

Influence of φ_0

In the next simulations we test the dependence of the motion on the unstressed position of the rotational spring φ_0. We fix $\mu = 0.4$ and $y_0 = 1$ m, and vary φ_0. Fig. 16 represents the motions for different values of φ_0 in the case $\varepsilon_N = 0.2$.

The numerical tests reveal that for $\varphi_0 < 0.23$ the mass m_1 never detaches from the surface and the motion consists of oscillations which tend alterna-

tively toward two accumulation points. The stick phase takes place when the velocity changes sign and also in the half period $\dot{s} < 0$, alternating to the slip phase (see Fig. 16(a)). In the half period $\dot{s} > 0$, the oscillation is in slip mode. For $\varphi_0 > 0.23$, the mass m_1 detaches from the moving surface. The motion exhibits free flight-slip-stick oscillations when $\dot{s} < 0$ and slip oscillations when $\dot{s} > 0$ (Fig. 16(b)). As φ_0 increases, the amplitudes of the oscillations reduce, and, consequently, the orbits occupy smaller and smaller regions in the $(\varphi, \dot{\varphi})$ plane (compare the length of the coordinate axes in the phase portraits of Fig. 16). The free-flight phase disappear when $0.375 < \varphi_0 < 0.430$ (Fig. 16(c)). When $0.43 < \varphi_0 < 0.48$ a small bounce per period takes place (Fig. 16(d)). For $\varphi_0 > 0.478$ (value previously found in the bifurcation diagrams of Fig. 6), the mass m_1 detaches from the surface and stays in equilibrium in free-flight.

Referring to the windscreen wiper application, these simulations suggest that the hopping phenomenon can depend on the permanent deformation of the wiper blade which affect the blade rubber when its elastic properties are compromised and irreversible plastic deformations occur. Therefore the phenomenon should be more frequent with old wipers, affected by a larger 'permanent deformation'.

Influence of y_0

Finally, we change the value of the unstressed configuration y_0 of the linear spring. We fix $\mu = 0.4$ and $\varphi_0 = 0.34$. As shown in Fig. 17, if we reduces the value of y_0 to 0.924, the bounces reduce in number and amplitude. For $y_0 = 0.739$, the free-flight phases disappear. When $\dot{s} > 0$, slip oscillations quickly converge toward the point $\varphi \simeq 0.58$ and, when $\dot{s} < 0$, stick-slip oscillations take place.

These results show that, again in the interpretation of the model as windscreen wiper, the hopping depends on the wiper metal arm, and it is enhanced when there is not enough (static) push on the rubber blade toward the glass.

7 Conclusions

A system with a varying number of degrees of freedom affected by geometric non-linearity and non-smoothness due to friction and impacts is investigated. The paper highlights how an apparently simple mechanical model (i) requires a complex set of transition conditions to link phases of motion

characterized by a varying number of governing equations, and (*ii*) possesses, as a consequence, a very complex dynamics where many different dynamical phenomena have been observed and related to the properties of the system. Both the non-smooth and the varying-dimension characters have been shown to play a key role.

It is clarified that the adopted mathematical framework is not fully consistent - a price to be paid to its relative simplicity. In the numerical code we developed for the simulations we insert appropriate warnings when various inconsistencies (or paradoxes) occur. In the numerical simulations shown in the paper we encounter only one of them.

In the case of constant driving velocity of a moving surface, the system dynamics is investigated for varying values of both the friction coefficient (μ) and the unstressed position of the rotational spring (φ_0). The bifurcation diagrams generated with a restitution coefficient in the normal direction equal to zero depict a wide variety of motions, and some of them were not highlighted in previous publications.

The introduction of a restitution coefficient in the normal direction different from zero allows a more realistic description of the system dynamics, accounting for bounces and a phenomenon in which the transition from free-flight to contact regime occurs through infinitely many impacts, named 'chattering'. Moreover, in the considered numerical simulations, in several situations this avoids the Painlevé paradox and the related jump of the reactive forces, and in some other cases it avoids the interruption of periodic bifurcation branches.

Finally some simulations are presented for the case of sinusoidal velocity of the moving surface. These simple examples seem to justify the adoption of the model under investigation to study the hopping phenomenon in windscreen wipers, for which it was originally developed.

Acknowledgement. This work has been developed in the framework of the international research project "Dynamics and control of engineering systems affected by friction forces" founded by the Royal Society of London. The authors thank Dr. Laura Marcheggiani for her help in the numerical simulations.

References

[1] M. di Bernardo, P. Kowalczyk, A. Nordmark, 2002, "Bifurcations of dynamical systems with sliding: derivation of normal form mappings," *Physica D*, **170**, 175205.

[2] C. Budd, F. Dux, 1994, "Chattering and Related Behaviour in Impact Oscillators," *Phil. Trans. R. Soc. Lond.*, **347**, 365-389.

[3] S.-C. Chang, H.-L. Pin, 2004, "Chaos attitude motion and chaos control in an automotive wiper system," *Int. J. Solids Struct.*, **41**, 3491-3504.

[4] H. Dankowicz, A. Nordmark, 2000, "On the origin and bifurcations of stickslip oscillations," *Physica D*, **136**, 280302.

[5] L. Demeio, S. Lenci, 2006, "Asymptotic analysis of chattering oscillations for an impacting inverted pendulum," *Quart. J. Mech. Appl. Math.*, **59**, 419-434.

[6] S. Foale, S. R. Bishop, 1992, "Dynamical Complexities of Forced Impacting Systems," *Phil. Trans. R. Soc. Lond.*, **338**, 547-556.

[7] U. Galvanetto, 2001, "Some discontinuous bifurcations in a two-block stickslip system," *J. Sound Vibr.*, **248**, 653669.

[8] S. Goto, H. Takahashi, T. Oya, 2001, "Clarification of the mechanism of wiper blade rubber squeal noise generation," *JSAE Review*, **22**, 57-62.

[9] N. Hinrichs, M. Oestreich, K. Popp, 1997, "Dynamics of oscillators with impact and friction," *Chaos, Sol. Fract.*, **8**, 535-558.

[10] J. B. Keller, 1985, "Impact with friction," *ASME J. Appl. Mech.*, **53**, 1-4.

[11] G. Lancioni, S. Lenci, U. Galvanetto, 2007, "The dynamics of a two-DOF system constrained by a frictional mono-lateral surface," Report of the Royal Society grant "Dynamics and control of Engineering systems affected by friction forces".

[12] R.I. Leine, B. Brogliato, H. Nijmeijer, 2002, "Periodic motion and bifurcations induced by the Painlevé paradox," *Eur. J. Mech. A/Solids*, **21**, 869-896.

[13] R.I. Leine, D.H. van Campen, 2006, "Bifurcation phenomena in non-smooth dynamical systems," *Eur. J. Mech. A/Solids*, **25**, 595616.

[14] R.I. Leine, H. Nijmeijer, 2004, *Dynamics and Bifurcations in Non-Smooth Mechanical Systems*, Lecture Notes in Applied and Computational Mechanics Vol. 18. Berlin Heidelberg New-York, Springer-Verlag.

[15] C. Liu, Z. Zhao, B. Chen, 2007, "The bouncing motion appearing in a robotic system with unilateral constraint," *Nonlinear Dynamics*, **49**, 217-232.

[16] A. Nordmark, 1991, "Non-periodic motion caused by grazing incidence in an impact oscillator," *J. Sound Vibr.*, **145**, 279-297.

[17] A. Nordmark, H. Dankowicz, A. Champneys, 2008, "Nonsmooth bifurcations in systems with impact and friction; I. discontinuities in the impact law," *preprint*.

[18] A. Nordmark, P. Piiroinen, 2009, "Simulation and stability analysis of impacting systems with complete chattering," to appear in *Nonlinear Dynamics*.

[19] S. Okura, 2000, "Dynamic analysis of blade reversal behavior in a windshield wiper system," *SAE Technical Paper Series 2001-01-0127*.

[20] E. Pavlovskaia, M. Wiercigroch and C. Grebogi, 2001, "Modeling of an impact system with a drift," *Phys. Review E*, **64**.

[21] F. Pfeiffer, C. Glocker, 1996 *Multibody dynamics with unilateral contacts*. John Wiley & Sons, Inc.

[22] F. Pfeiffer, M.O. Foerg, 2005, "On the structure of multiple impact system," *Nonlinear Dynamics*, **42**, 101-112.

[23] R. Suzuki, K. Yasuda, 1998, "Analysis of Chatter Vibration in an Automotive Wiper Assembly," *Int. J. Jap. Soc. Mech. Eng.*, serie C, **41**, 616-620.

[24] Z. Zhao, C. Liu, W. Ma, B. Chen, 2008, "Experimental investigation of the Painlevé paradox in a robotic system," *ASME J. Appl. Mech.*, **75**, 041006.

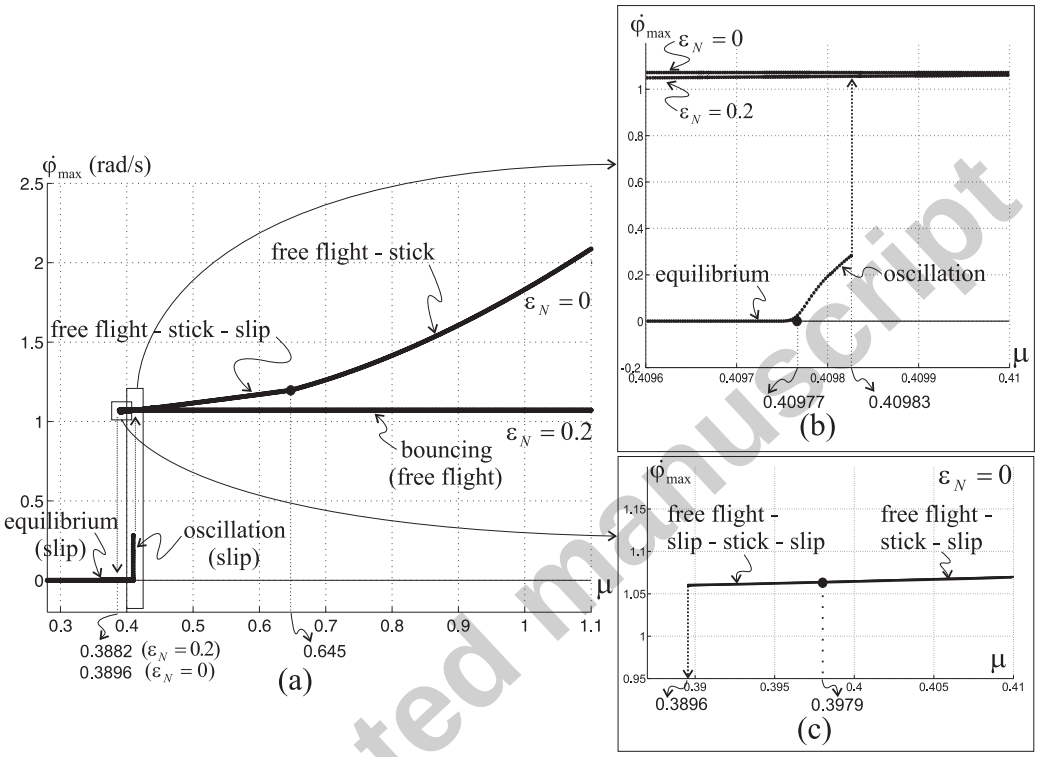

Figure 2: Simulation 1. Bifurcation diagrams for varying μ.

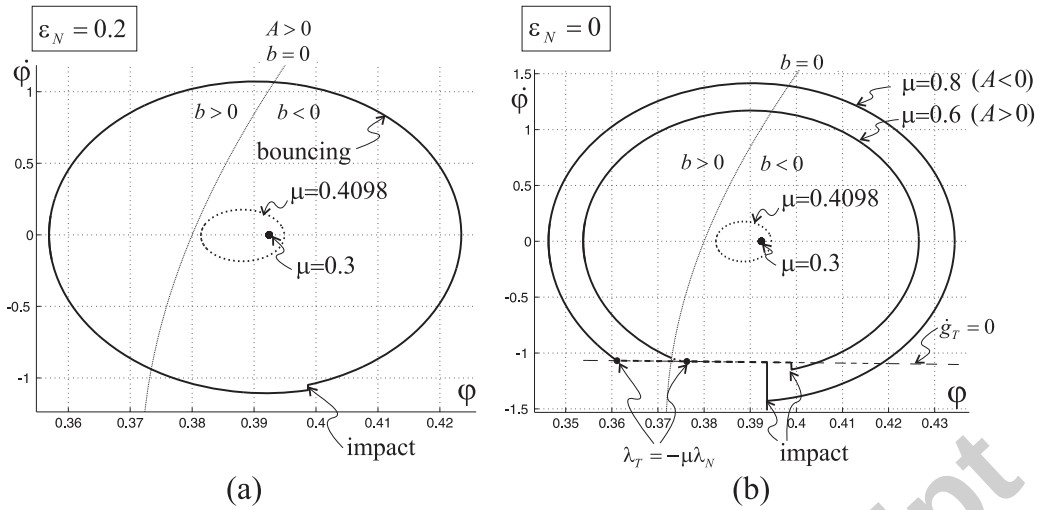

Figure 3: Simulation 1. Orbits in the $\varphi - \dot{\varphi}$ phase plane. Free-flight ≡ solid line; slip ≡ dotted line; stick ≡ dashed line.

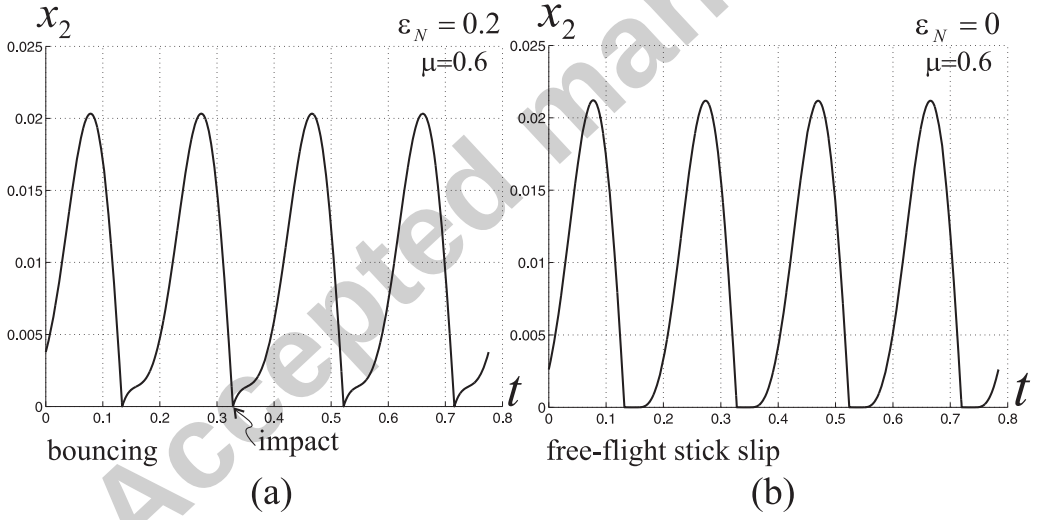

Figure 4: Simulation 1. Vertical displacement x_2 of m_1 as function of time t in the periodic motions obtained when $\mu = 0.6$.

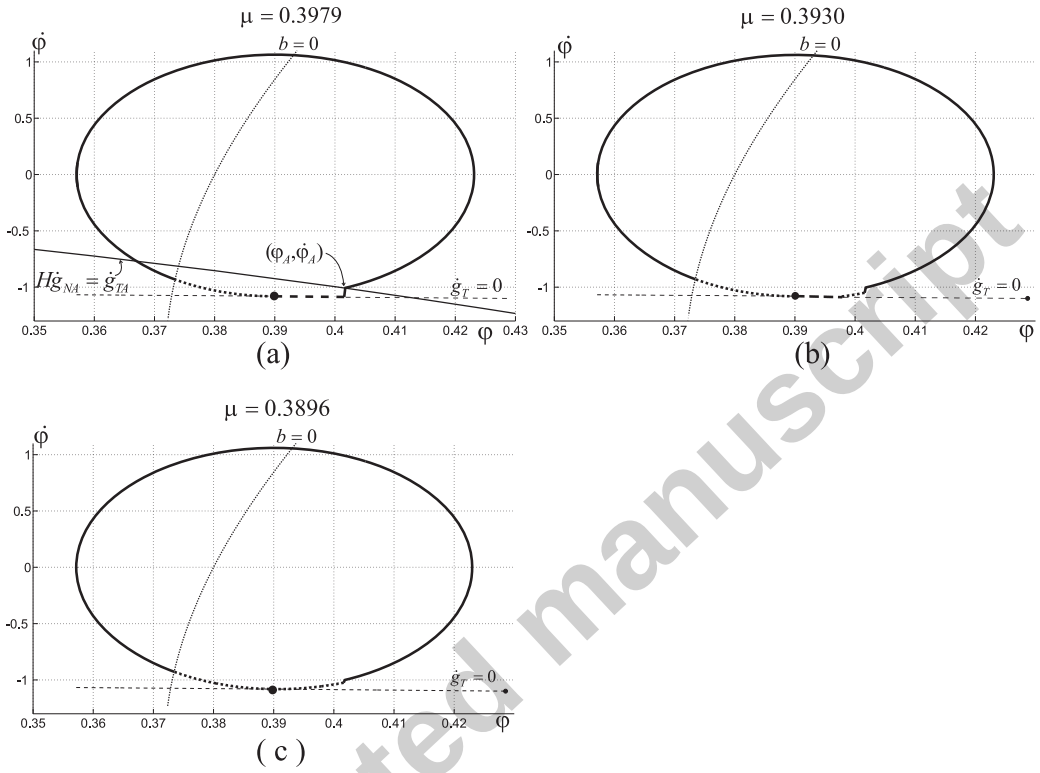

Figure 5: Simulation 1. Orbits in the $\varphi - \dot{\varphi}$ phase plane. Free-flight $\equiv$ solid line; slip $\equiv$ dotted line; stick $\equiv$ dashed line.

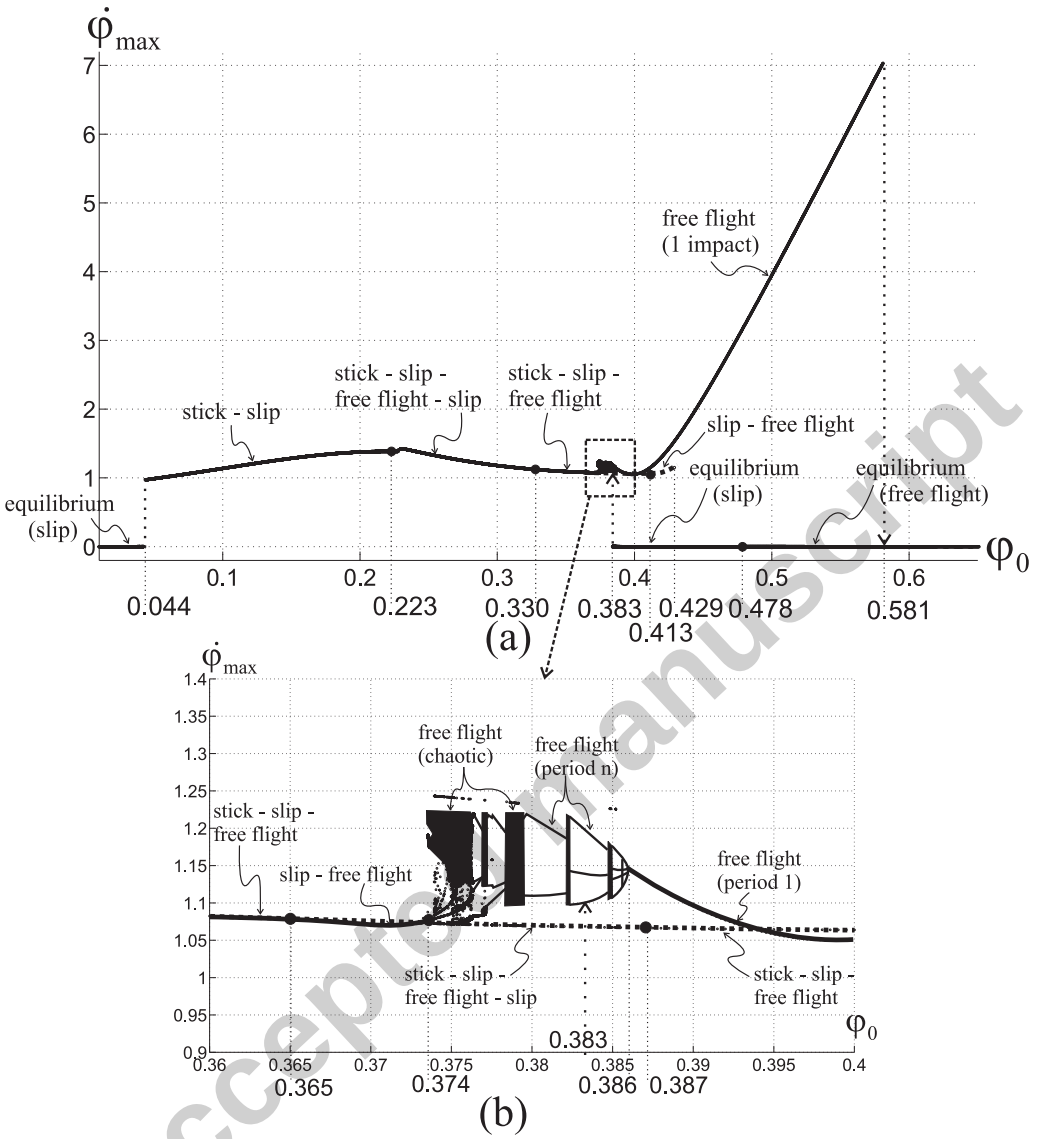

Figure 6: Simulation 1. (a) bifurcation diagrams for varying φ_0. $\varepsilon_N = 0.2 \equiv$ solid line; $\varepsilon_N = 0 \equiv$ dashed line. (b) zoom of a portion of figure (a).

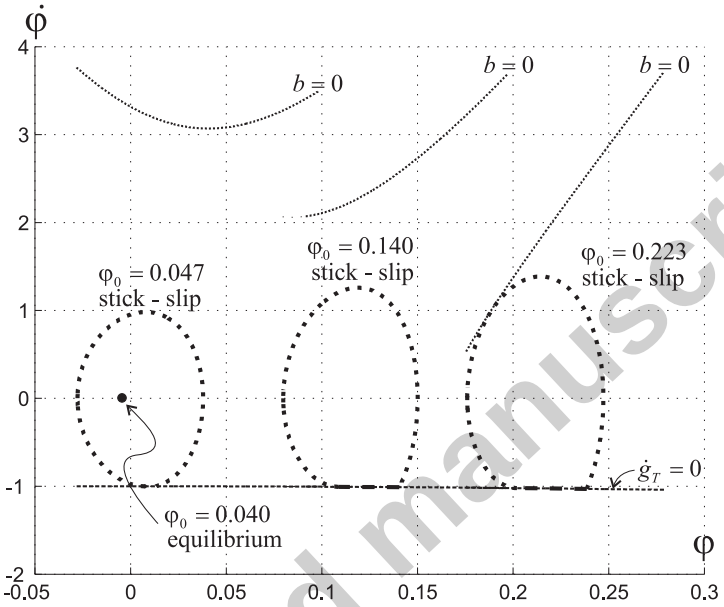

Figure 7: Simulation 1. Laid motions. Orbits in the $\varphi - \dot{\varphi}$ phase plane. Slip $\equiv$ dotted line; stick $\equiv$ dashed line.

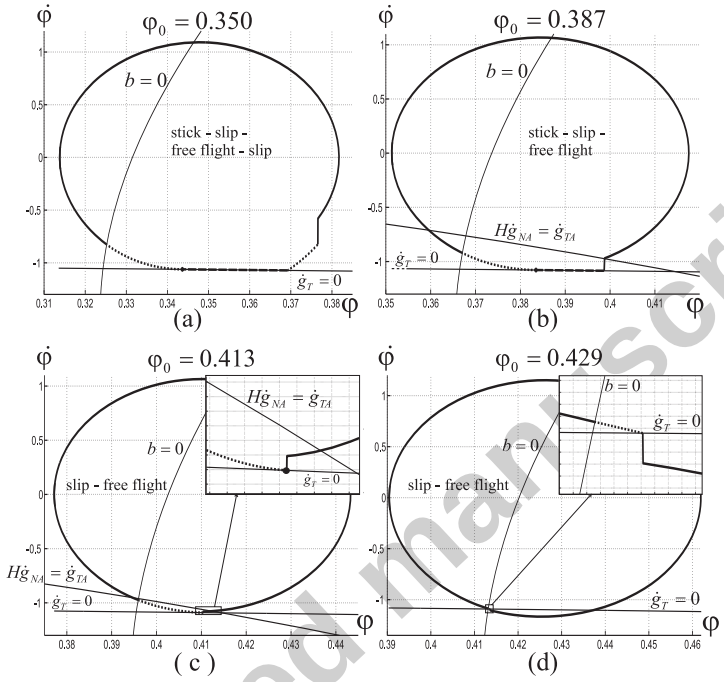

Figure 8: Simulation 1. Case of plastic impact ($\varepsilon_N = 0$). Orbits in the $\varphi - \dot{\varphi}$ phase plane. Free-flight $\equiv$ solid line; slip $\equiv$ dotted line; stick $\equiv$ dashed line.

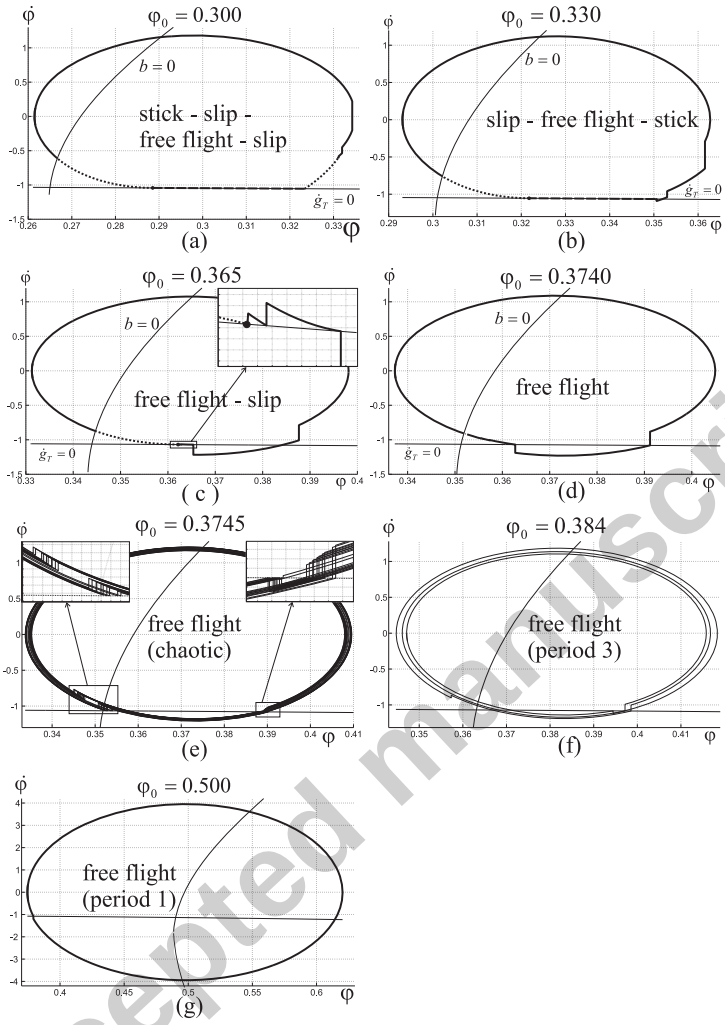

Figure 9: Simulation 1. Case of elasto-plastic impact ($\varepsilon_N = 0.2$). Orbits in the $\varphi - \dot{\varphi}$ phase plane. Free-flight $\equiv$ solid line; slip $\equiv$ dotted line; stick $\equiv$ dashed line.

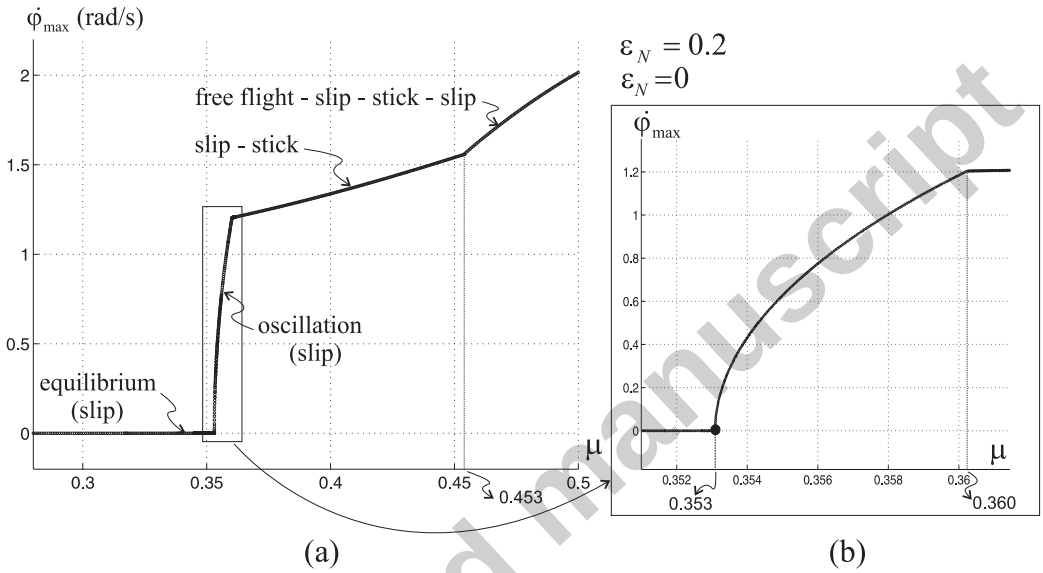

Figure 10: Simulation 2. Bifurcation diagrams for varying μ.

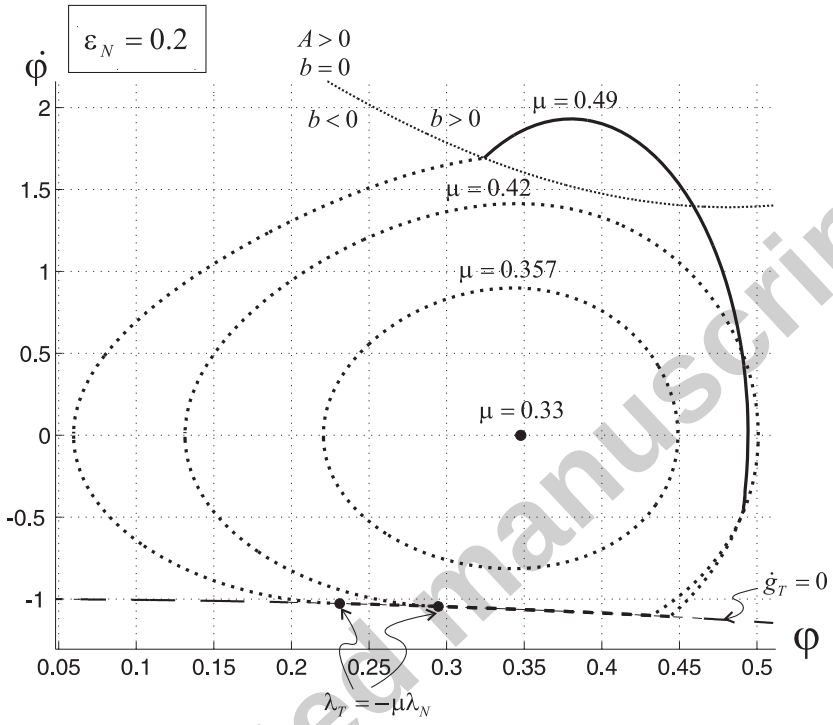

Figure 11: Simulation 2. Orbits in the $\varphi - \dot{\varphi}$ phase plane. Free-flight $\equiv$ solid line; slip $\equiv$ dotted line; stick $\equiv$ dashed line.

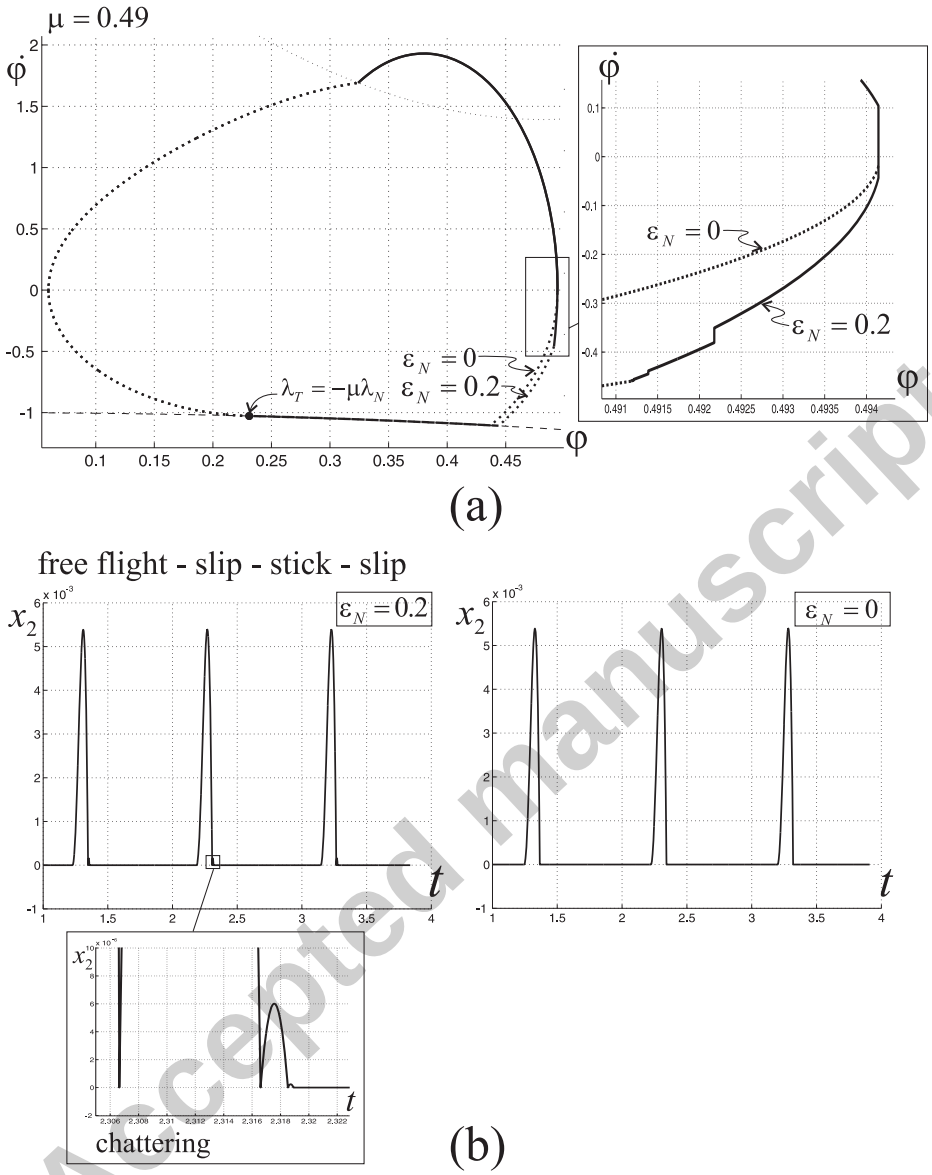

Figure 12: Simulation 2. Orbits in the $\varphi - \dot{\varphi}$ phase plane and time histories.

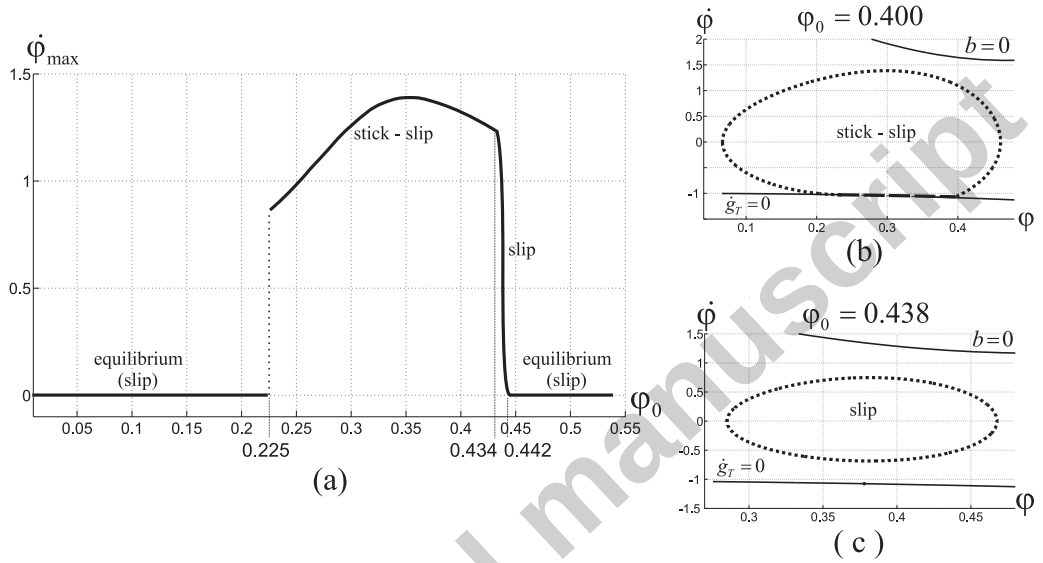

Figure 13: Simulation 2. (a): bifurcation diagrams for varying φ_0; (b)-(c): orbits for fixed values of φ_0.

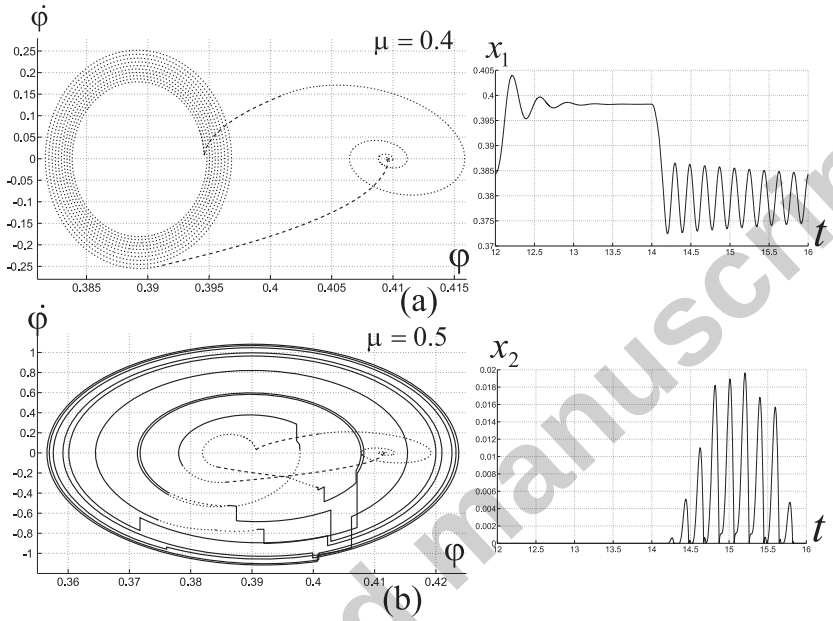

Figure 14: Sinusoidal surface velocity. Phase portraits and time histories for: (a) $\mu = 0.4$, (b) $\mu = 0.5$.

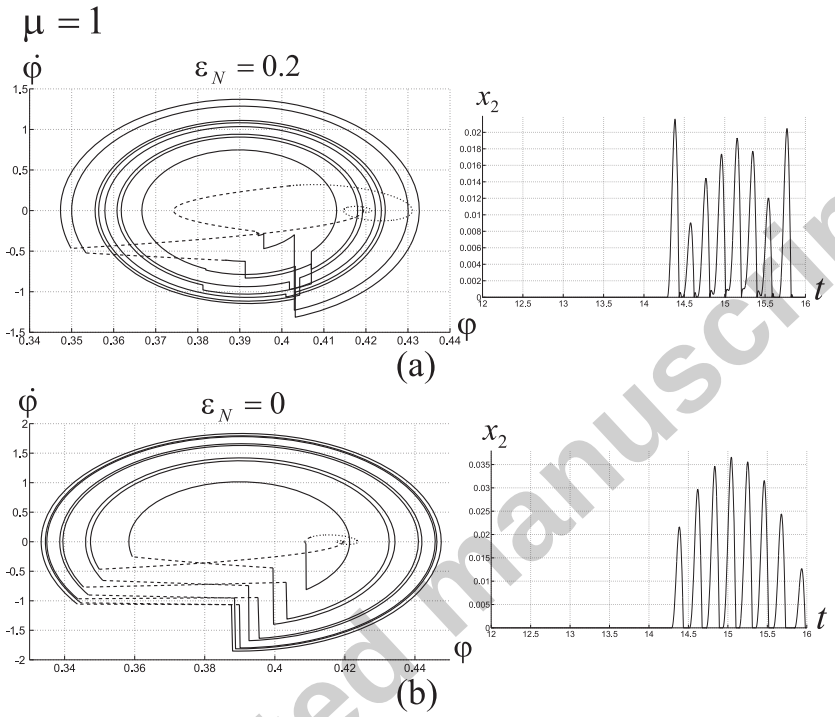

Figure 15: Sinusoidal surface velocity. Phase portraits and time histories for $\mu = 1$: (a) $\varepsilon_N = 0.2$, (b) $\varepsilon_N = 0$.

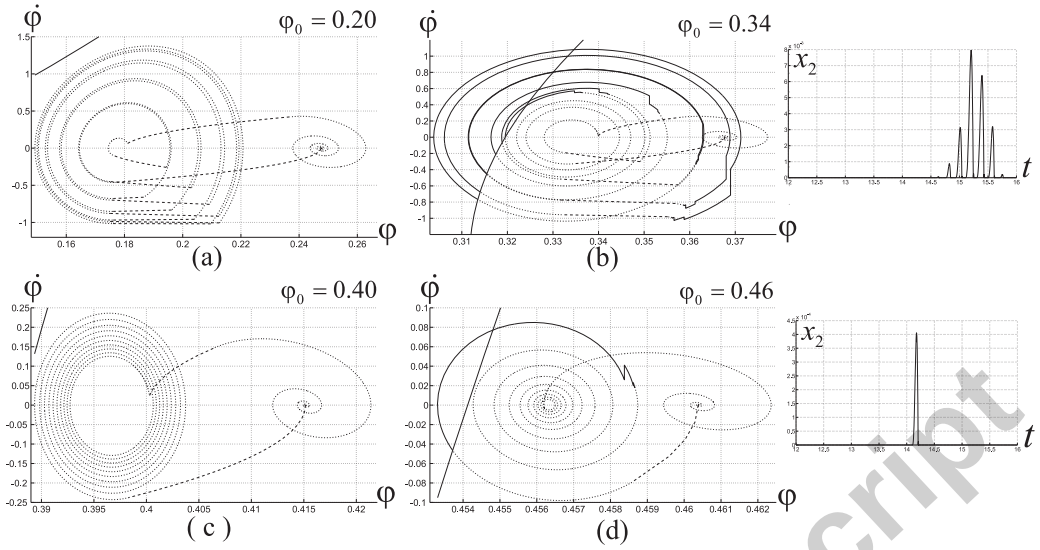

Figure 16: Sinusoidal surface velocity. Phase portraits and time histories for: (a) $\varphi = 0.20$, (b) $\varphi = 0.34$ (c) $\varphi = 0.40$, (d) $\varphi = 0.46$. $\varepsilon_N = 0.2$.

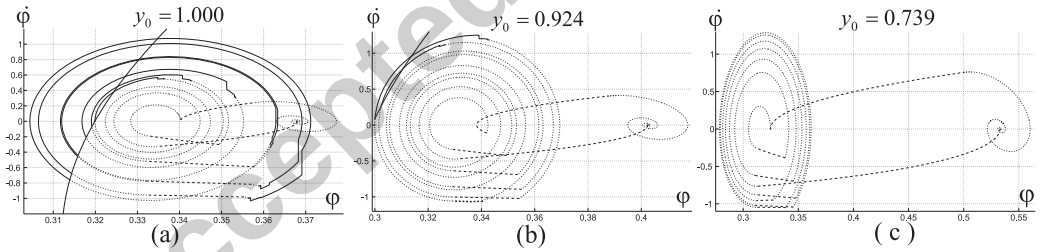

Figure 17: Sinusoidal surface velocity. Phase portraits for: (a) $y_0 = 1$, (b) $y_0 = 0.924$, (c) $y_0 = 0.739$.